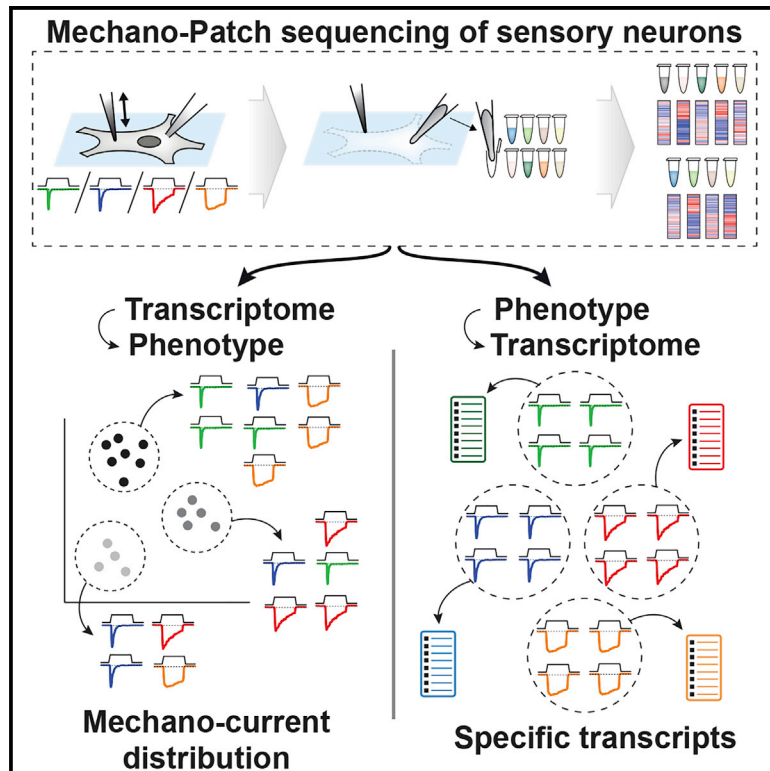


Patch-seq of mouse DRG neurons reveals candidate genes for specific mechanosensory functions

Graphical abstract



Authors

Thibaud Parpaite, Lucie Brosse, Nina Séjourné, Amandine Laur, Yasmine Mechioukhi, Patrick Delmas, Bertrand Coste

Correspondence

bertrand.coste@univ-amu.fr

In brief

Mechanosensation is the least understood sensory modality at the molecular level. Parpaite et al. combine single-cell RNA sequencing with mechanosensitive current recordings in cultured sensory neurons. One-to-one correspondence between mechanoelectric properties and single-cell transcriptomes provides a valuable resource for the identification of molecular factors involved in mechanosensation.

Highlights

- Patch-seq is performed on mechanically characterized DRG sensory neurons
- Transcriptomically defined neuronal classes and current subtypes are correlated
- Datasets of specific transcripts of current subtype-expressing neurons are generated
- TACAN (*Tmem120a*) and Tentonin-3 (*Tmem150c*) do not contribute to DRG mechano-currents



Article

Patch-seq of mouse DRG neurons reveals candidate genes for specific mechanosensory functions

Thibaud Parpaite,^{1,2} Lucie Brosse,^{1,2} Nina Séjourné,¹ Amandine Laur,¹ Yasmine Mechioukhi,¹ Patrick Delmas,¹ and Bertrand Coste^{1,3,*}

¹Aix Marseille Université, CNRS, LNC-UMR 7291, 13344 Marseille, France

²These authors contributed equally

³Lead contact

*Correspondence: bertrand.coste@univ-amu.fr

<https://doi.org/10.1016/j.celrep.2021.109914>

SUMMARY

A variety of mechanosensory neurons are involved in touch, proprioception, and pain. Many molecular components of the mechanotransduction machinery subserving these sensory modalities remain to be discovered. Here, we combine recordings of mechanosensitive (MS) currents in mechanosensory neurons with single-cell RNA sequencing. Transcriptional profiles are mapped onto previously identified sensory neuron types to identify cell-type correlates between datasets. Correlation of current signatures with single-cell transcriptomes provides a one-to-one correspondence between mechanoelectric properties and transcriptomically defined neuronal populations. Moreover, a gene-expression differential comparison provides a set of candidate genes for mechanotransduction complexes. *Piezo2* is expectedly found to be enriched in rapidly adapting MS current-expressing neurons, whereas *Tmem120a* and *Tmem150c*, thought to mediate slow-type MS currents, are uniformly expressed in all mechanosensory neuron subtypes. Further knockdown experiments disqualify them as mediating MS currents in sensory neurons. This dataset constitutes an open resource to explore further the cell-type-specific determinants of mechanosensory properties.

INTRODUCTION

Mechanosensory neurons are involved in multiple sensory modalities, including innocuous tickle, pleasant and discriminative touch, proprioception, and kinesthesia as well as various mechanical pain-related sensations such as sharp or deep aching pain and visceral pain. A rich variety of dedicated dorsal root ganglion (DRG) mechanosensory neurons and structured endings innervate our skin, mucosa, muscles, tendons, and joints to initiate these mechanosensory sub-modalities (Abraira and Ginty, 2013; Proske and Gandevia, 2012; Roudaut et al., 2012). Physical cues are detected at the sensory nerve endings/auxiliary cells, where specialized mechanosensitive (MS) ion channels convert mechanical stimuli into electrochemical signals (Basbaum et al., 2009; Kefauver et al., 2020).

The discovery from low-throughput patch-clamp screening of PIEZO proteins as genuine force-sensing channels has provided better understanding of mechanical force transduction mechanisms in somatosensory neurons (Coste et al., 2010) as well as in multiple biological systems (Murthy et al., 2017; Wu et al., 2017). PIEZO1 and PIEZO2 form a unique class of a conserved family of nonselective cation channels that are activated by physical stimuli, including pressure, stretch, and shear stress (Coste et al., 2012; Ranade et al., 2014a). Both channels generate MS currents with rapid inactivation that convert force

into cellular responses on a millisecond timescale. While PIEZO1 is broadly expressed in non-neuronal tissues exposed to pressure and fluid flow, e.g., kidneys, bladder, endothelial cells, and blood cells, PIEZO2 is predominantly expressed in sensory tissues, such as DRG, trigeminal ganglia, and Merkel cells (Murthy et al., 2017; Wu et al., 2017). PIEZOs are co-expressed in nodose and petrosal sensory ganglia where they are shown to be involved in baroreceptor reflex (Min et al., 2019; Zeng et al., 2018). Studies from knockout (KO) mouse models have shown that *Piezo2* plays a crucial role in innocuous touch sensation (Ranade et al., 2014b) and proprioception (Florez-Paz et al., 2016; Woo et al., 2015). *Piezo2* also plays a more marginal role in mechanical nociception (Murthy et al., 2018b; Szczot et al., 2018). These functions appeared to be conserved in humans, as patients with loss-of-function variants in *PIEZO2* show deficits in touch discrimination and joint proprioception, and failed to develop mechanical allodynia after skin inflammation (Chesler et al., 2016; Szczot et al., 2018).

DRG neurons express a large repertoire of excitatory MS currents classified as rapidly adapting (RA), intermediately adapting (IA), and slowly/ultra slowly adapting (SA/ultra SA) currents, according to their inactivation kinetics to sustained mechanical stimulation (Coste et al., 2010; Drew et al., 2002, 2004; Francois et al., 2015; Hao and Delmas, 2010; Hu and Lewin, 2006; Ranade et al., 2014b; Rugiero et al., 2010). It is now well established that



PIEZO2 channels sustain RA MS currents (Coste et al., 2010; Ranade et al., 2014b). Importantly, IA and slow-type MS currents are largely unaffected in *Piezo2* KO DRG neurons (Ranade et al., 2014b), demonstrating that as-yet-unknown MS channels must account for the other MS currents. It is worthwhile to identify these channels since many sensations related to innocuous and noxious mechanical stimuli are independent from *PIEZO2* in humans (Case et al., 2021; Chesler et al., 2016; Szczot et al., 2018). Recently, two other genes, namely, *Tmem120a* (Tacan) and *Tmem150c* (Tentonin 3), have been proposed to encode ion channels sustaining slow MS currents in DRG neurons (Beaulieu-Laroche et al., 2020; Hong et al., 2016), but some of these findings are controversial (Anderson et al., 2018; Dubin et al., 2017). Hence, despite significant advances, the full panel of MS channels involved in mechanosensation has yet to be established.

Identification of MS channels is hampered by the large heterogeneity of DRG and trigeminal sensory neurons. This heterogeneity has been well documented by large-scale single-cell transcriptomics enabling gene-expression-based classification (Li et al., 2016; Nguyen et al., 2019; Renthal et al., 2020; Sharma et al., 2020; Usoskin et al., 2015; Zeisel et al., 2018). Eight main classes of DRG sensory neurons have been identified, including low-threshold mechanoreceptors, proprioceptors, thermoreceptors, nociceptors, itch-sensitive neurons, and type C low-threshold mechanoreceptors, which can be further subdivided into up to 17 clusters identified transcriptionally (Zeisel et al., 2018). A limitation of large-scale classification based on unsupervised grouping of neurons with similar expression profiles is the lack of direct functional correlates. Indeed, this would require a prior functional characterization of individual neurons by patch-clamp experiments, a laborious step incompatible with large samples of neurons. Nevertheless, the direct correlation of single-cell transcriptomes with functional mechanosensory properties could serve as a basis for identifying the genes involved in mechanotransduction.

Here, we used Patch-seq methodology (Cadwell et al., 2016; Fuzik et al., 2016) to combine recordings of MS currents in cultured mouse DRG neurons with single-cell RNA sequencing (scRNA). *In silico* analysis of collected data with a previous large-scale dataset allowed to link MS current subtypes to molecular neuronal clusters. These data made it possible to precise the distribution of the four different types of MS currents in molecularly defined populations of DRG neurons. Moreover, differential comparison provided a list of candidate genes for mechanotransduction complexes. This dataset combining patch-clamp electrophysiology and quantitative scRNA-seq constitutes an open resource to explore further the cell-type-specific determinants of mechanosensory properties.

RESULTS

Coupling patch-clamp recording of MS currents with scRNA-seq

To identify molecular features associated with specific MS phenotypes, we combined single-cell RNA-sequencing (scRNA-seq) profiling with electrophysiological characterization of MS currents in individual DRG neurons. A representation of the methodological procedure used for data collection is depicted

in Figure 1A. Briefly, sensory neurons from mouse DRG cultures were recorded using the whole-cell patch-clamp mode in order to characterize the properties of excitatory MS currents in response to cell poking with a mechanical probe (Coste et al., 2007, 2010; Drew et al., 2002; Hao and Delmas, 2010; Hu and Lewin, 2006; McCarter et al., 1999; Michel et al., 2020; Rugiero et al., 2010). After functional characterization, the content of each cell was harvested through the recording pipette prior to the generation of cDNA libraries and RNA-seq (see STAR Methods for detailed procedure). Using this approach, we selected 62 DRG neurons covering the main types of MS currents (Figure 1B) for cDNA library preparation, of which 53 cells proved suitable for scRNA-seq analysis. A total of 1.6 billion paired-end reads were generated, among which 1.4 billion were correctly aligned to mouse genome, giving an average of 25.9 million mapped reads for a given neuron. The mean number of detectable genes per cell was $13,359 \pm 1,478$. Analysis of reference genes showed no differences between samples, which attested the absence of batch effect between the sequencing runs (Figure S1A). Quality metrics values from sequenced neurons were within the same range than large-scale DRG scRNA-seq studies (Li et al., 2016; Usoskin et al., 2015; Zeisel et al., 2018), attesting that patch-clamping/poking the neurons prior to RNA-seq analysis did not impact gene detection (Figure S1B). Overall, the depth of our molecular analysis allowed us to quantitatively assay the expression of genes in each DRG neuron and to compare expression differences of any of these genes in light with mechanical properties.

Categorization of MS current-expressing neurons prior to transcriptome profiling

To tentatively classify mechanosensory neurons based on their mechanical properties, we examined the kinetics of MS currents over a large population of mouse DRG neurons ($n = 312$), not intended for scRNA-seq. Previous studies have identified 3 to 4 kinetically distinct MS currents in rat and mouse DRG neurons, which may reflect the activation of non-uniform populations of ion channels (Coste et al., 2010; Drew et al., 2002, 2004; Francois et al., 2015; Hao and Delmas, 2010; Hu and Lewin, 2006; Ranade et al., 2014b; Rugiero et al., 2010). Based on exponential fit of inactivation kinetics, we identified four kinetically distinct MS currents with Gaussian mean value centered at 5.9 ± 1.6 , 15.1 ± 4.5 , 75.4 ± 13.8 , and 200.9 ± 66.8 ms (mean \pm SD) (Figure 1B). These currents were referred hereafter as rapidly adapting (RA; $\tau_{inac} \leq 10$ ms), intermediately adapting (IA; $10 \text{ ms} < \tau_{inac} \leq 30$ ms), slowly adapting (SA; $30 \text{ ms} < \tau_{inac} \leq 110$ ms), and ultra-SA ($\tau_{inac} > 110$ ms). Prototypical recordings of these currents are depicted in Figure 1C. It is worth noting that a substantial part of mechanosensory DRG neurons exhibited more than one single-current component, potentially reflecting the activation of two or more populations of distinct MS channels. For analytical purpose, we only considered mixed currents best fitted by bi-exponential functions. The contribution of each component to the whole MS current was estimated from the amplitude of the respective exponential fit (Figure S2, see STAR Methods for detailed procedure). Representative examples of biphasic currents classified as RA/SA, RA/ultra-SA, and IA/ultra-SA are illustrated in Figure 1D.

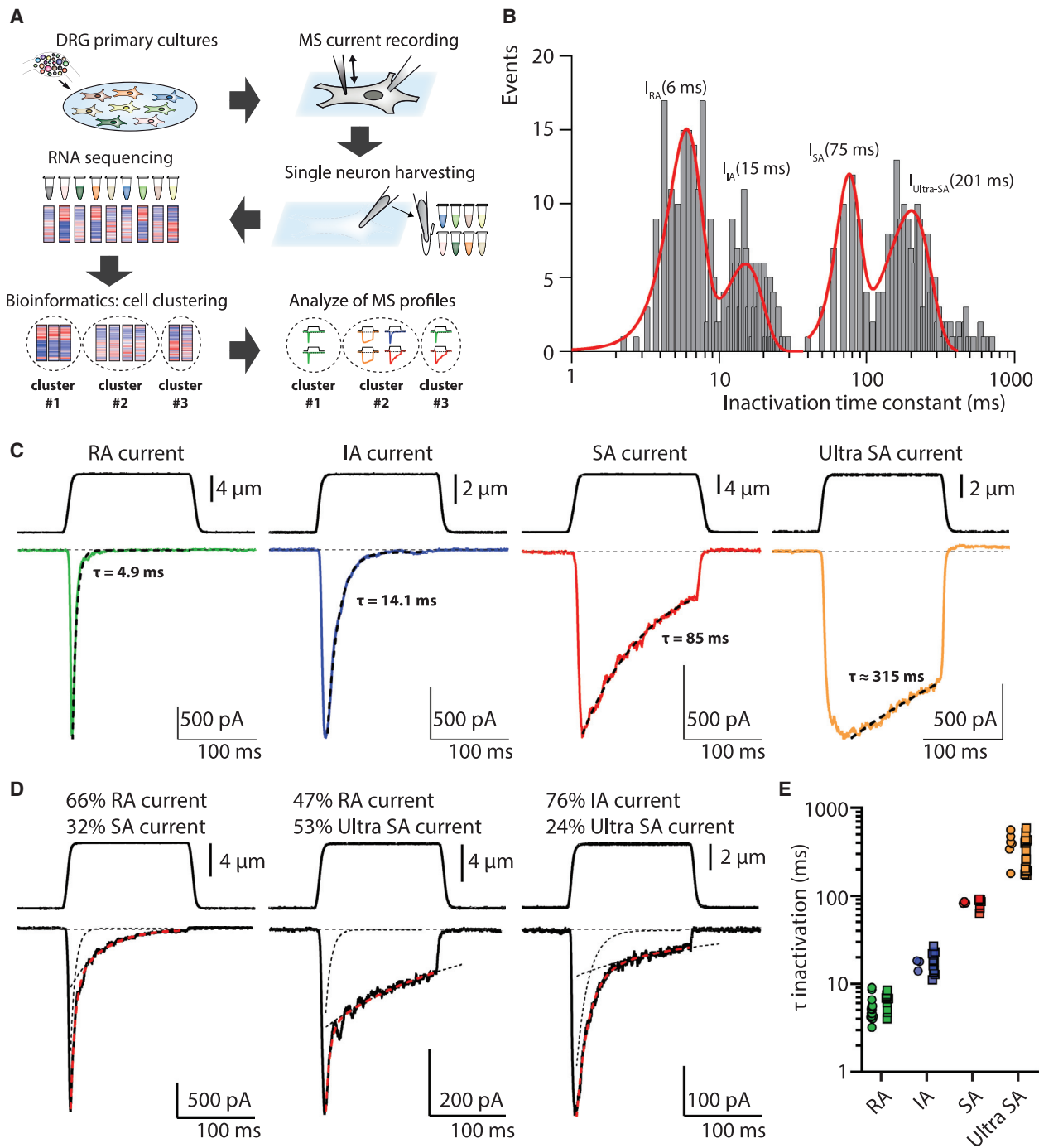


Figure 1. Single-cell RNA-seq coupled to MS current characterization

(A) Schematic representation of the methodology used in this study.

(B) Frequency distribution of the inactivation time constants determined from mono- and bi-exponential fits of MS currents. Data were collected over 312 DRG neurons. Bin width was 0.5 ms for I_{RA} and I_{IA} , and 10 ms for I_{SA} and $I_{Ultra-SA}$.

(C) Representative examples of the distinct types of MS currents with inactivation time course fitted with a mono-exponential function (black dashed line).

(D) Examples of MS currents fitted with bi-exponential functions (red dashed line). Black dashed lines show each mono-exponential component extracted from the fit.

For (C) and (D), top traces represent the mechanical probe displacement and bottom traces the recorded currents at -80 mV.

(E) Inactivation time-constant (τ) for all identified current components in scRNA-seq neurons with monophasic (circle) or biphasic (square) MS currents, $n = 53$ neurons from 16 mice.

This kinetics-based categorization made it possible to classify our successfully sequenced DRG neurons. Thus, from our sample of 53 scRNA-seq neurons, 49% displayed a monophasic MS current, while the remaining 45.5% showed a mixed current, with variable MS current components. Only 3 scRNA-seq neurons were unresponsive to mechanical stimulus, but this does not reflect physiological proportion (Coste et al., 2010; Hu and Lewin, 2006). Average values of τ_{inac} were 5.9 ± 0.3 , 18.8 ± 1.4 , 82.2 ± 2.8 , and 347.7 ± 26.5 ms for RA, IA, SA, and ultra-SA current, respectively ($n = 26, 15, 10, \text{ and } 24$; mean \pm SEM) (Figure 1E). The detailed profiles of MS currents in individual neurons are described in Table S1.

Mapping Patch-seq transcriptomes of MS neurons to single-cell RNA-seq datasets

Previous scRNA-seq studies performed on large samples of neurons have used gene-expression profile analysis to sort out DRG neurons into molecularly defined neuronal subclasses (Li et al., 2016; Sharma et al., 2020; Usoskin et al., 2015; Zeisel et al., 2018). To achieve high-quality classification of our neuron sample, we merged our data with the dataset of 1580 scRNA-seq DRG neurons from Zeisel and collaborators, which is available as open source (Zeisel et al., 2018). Then, we performed a joint analysis using mutual nearest neighbors (MNNs) correction by focusing on the expression magnitude of the 211 most highly enriched genes across DRG neuron clusters (Zeisel et al., 2018) (Figure S1C). This procedure allowed us to classify each neuron from our sample in transcriptional clusters identified previously (Zeisel et al., 2018) (Table S1). The merged datasets were mapped using t-distributed stochastic neighbor embedding (tSNE) projection (Figure 2A). Neurons from our sample spread across seven out of eight functionally distinct DRG neuron populations, some of which are composed of multiple transcriptional clusters whose functional specificity remains to be determined. Eight neurons were classified into the NF group of neurons typically considered as low-threshold mechanoreceptors (LTMRs) and proprioceptors. Six neurons belong to NP1 population related to polymodal nociceptors, whereas eleven neurons were assigned to NP2 population and a single neuron to NP3 population, which are related to itch-specific sensory neurons (Cavanaugh et al., 2009; Dong and Dong, 2018; Han et al., 2013; Wang and Zylka, 2009). Nine neurons were assigned to PEP1, a population of C-type thermo-nociceptors, and 16 neurons to PEP2, a population of lightly myelinated A δ nociceptors (Usoskin et al., 2015). Two neurons segregated into TH neuron population, representing C-low threshold mechanoreceptors (C-LTMRs), which contribute to pleasant touch (Li et al., 2011; Olsson et al., 2010) and mechanical allodynia (Seal et al., 2009). Finally, none of our scRNA-seq neurons belong to TrpM8 population. These neurons represent a labeled line for cold sensation, and their genetic ablation in mice has no effect on mechanical behaviors (Knowlton et al., 2013).

Expression of marker genes and genes coding for thermosensitive and pruriceptive molecular sensors confirmed the appropriate mapping of scRNA-seq neurons from our sample (Figures 2B and 2C). NF LTMRs and proprioceptors express the specific markers *Nefh* (neurofilament heavy chain), *Pvalb* (parvalbumin), *Calb1* (calbindin1), and *Ntrk2* and *Ntrk3* (TrkB and C), but

thermosensitive and pruriceptive itch molecular sensors were not detected. NP1-3 sensory neurons express *P2rx3* (P2X3), *PlexnC1* (plexin C1), and *Necab2* (N-terminal EF-hand calcium binding protein 2). The itch-related genes *Lpar3* and *Lpar5* (lysophosphatidic acid receptors 3 and 5) and *Mrgprd* (MRGPRD) are expressed in NP1 neurons, whereas NP2 population expresses *Mrgpra3* and *Mrgprx1* (MRGPRA3 and X1). PEP neurons express *Calca* (CGRP) and *Kit* (c-Kit) but differ in the expression of *Gal* (galanin prepropeptide) for PEP1 C-type thermo-nociceptors and *Nefh* for PEP2 lightly myelinated A δ nociceptors. The heat noxious sensors *Trpa1*, *Trpv1*, and *Trpm3* (Vandewauw et al., 2018) were strongly detected in NP1, NP2, and PEP1 C-type neurons compared with PEP2 A δ -type neurons. This is consistent with previous observation in skin-nerve recording studies that showed a higher proportion of C-type than A δ -type fibers that respond to noxious heat (Cain et al., 2001; Koltzenburg et al., 1997). Finally, the TH C-LTMRs characterized by expression of *Th* (tyrosine hydroxylase), *Fam19a4* (TFAFA4), and *Slc17a8* (Vglut3) are devoid of thermosensitive or itch-related molecular sensors.

Distribution of MS currents in genetically defined DRG subclasses

The characterization of MS current types expressed in scRNA-seq neurons allowed us to examine their distribution in transcriptionally defined DRG populations (Figures 3A and 3B). Except for NF neurons, which exhibited almost exclusively the RA current, all other molecularly defined DRG subclasses displayed more than one type of MS current. However, the prevalence of each current component differed among DRG groups. The Figure 3C shows the proportion of each MS current type in transcriptionally defined DRG neuron populations. The polymodal nociceptor NP1 subclass displayed all four types of MS currents, with individual contributions ranging from 10% to 33%. The itch-specific NP2 subclass expressed almost no SA current and showed a higher amount of RA current (42%) compared with IA and ultra-SA currents (35% and 20%, respectively). The C-type thermo-nociceptor PEP1 subclass had prominent IA current (56%), a lower amount of RA current (33%), with no or little SA and ultra-SA current components, respectively. The A δ nociceptor PEP2 subclass almost lacked IA current and expressed prominent ultra-SA current (39%) and robust RA and SA currents (34% and 23%, respectively). Finally, C-LTMR TH neurons showed both RA and ultra-SA currents. Although our small sample size precluded definite conclusion about the nature of MS current in C-LTMR TH neurons, our data are consistent with previous work indicating that TH neurons mainly express RA and ultra-SA currents, or a mixture of both (Delfini et al., 2013). Altogether, these results revealed that the genetically defined DRG subclasses have different complements of MS currents, which may reflect some heterogeneity and functional differences within a given DRG subclass.

Expression analysis of genes hypothesized to encode MS channels

It has been remarkably difficult to identify candidate excitatory MS channels in mammals. With the notable exception of PIEZO2 and of TMCs in auditory hair cells (Corey et al., 2019), other

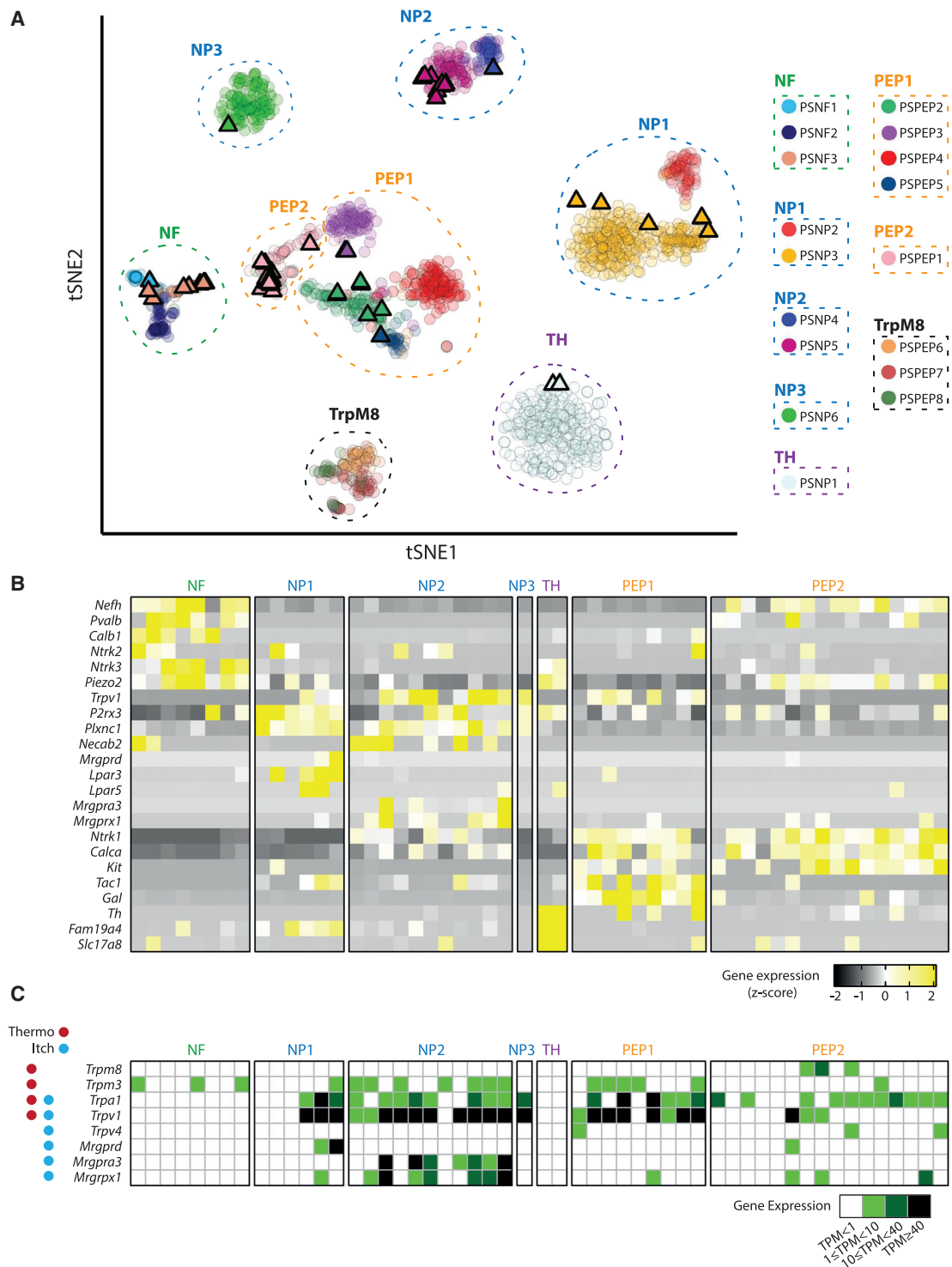


Figure 2. Cluster analysis of scRNA-seq neurons

(A) Visualization using t-SNE embedding of all cells colored by cluster identity. Triangles represent the scRNA-seq neurons of this study and circles the neurons from the study of Zeisel and collaborators. Main populations of neurons are surrounded by dashed lines. See [Figure S1C](#) for the heatmap of the expression of genes used for joint analysis.

(B) Heatmap of expression of marker genes in neurons grouped by population.

(C) Expression level of genes coding for thermosensitive and pruriceptive molecular sensor neurons grouped by population. NF, neurofilament; NP, non-peptidergic; TH, tyrosine hydroxylase; PEP, peptidergic.

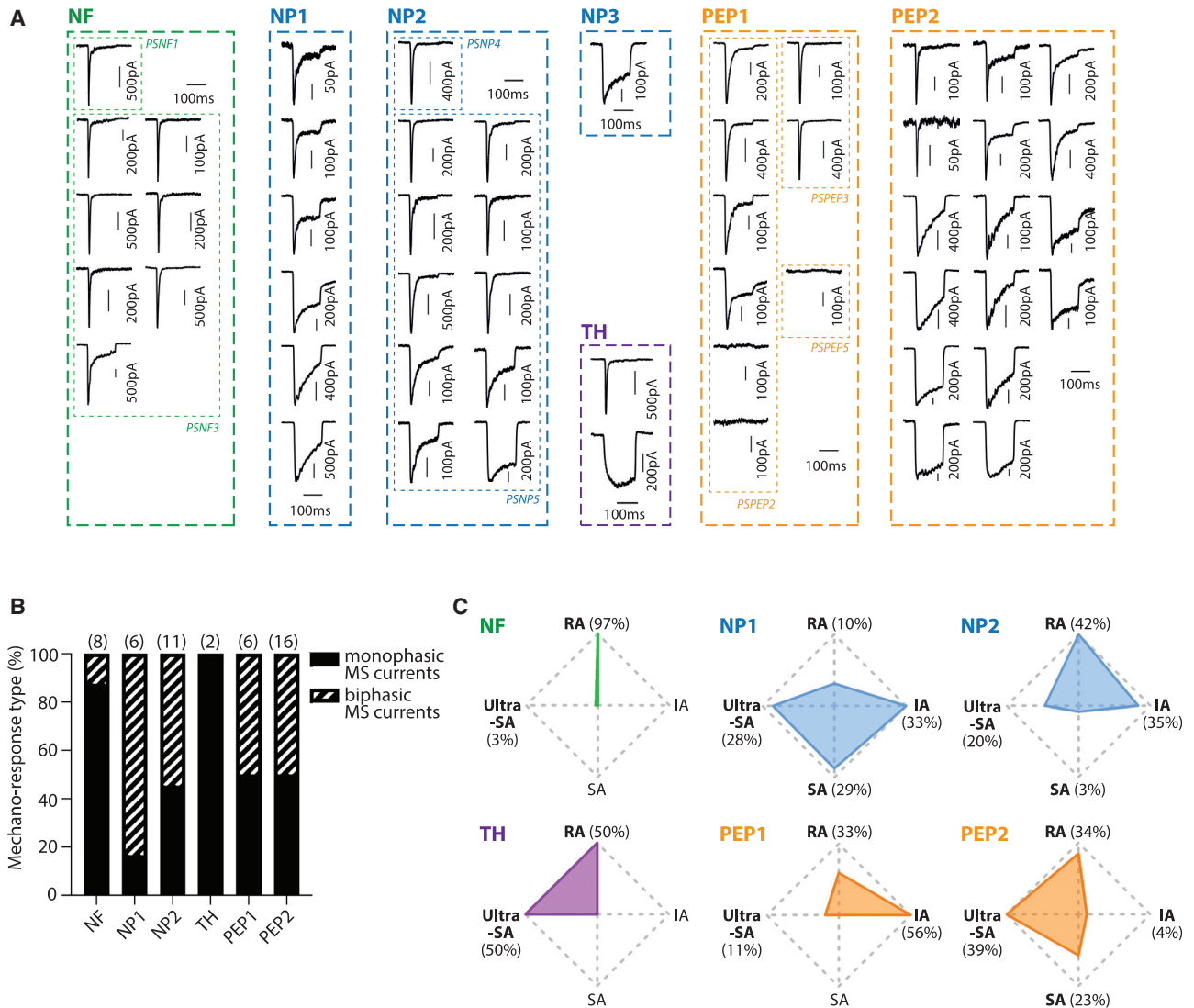


Figure 3. Distribution of MS currents among transcriptional clusters of DRG neurons

(A) Traces of MS currents recorded in the scRNA-seq neurons and grouped by neuronal transcriptional population. Mechanical stimulation traces are not shown for clarity's sake.

(B) Proportion of MS neurons expressing monophasic and biphasic MS currents in each population. Number of neurons for each population is in brackets.

(C) Relative contribution of MS current types to the total MS current in each population. Numbers of neurons are as in (B).

putative candidates have not been confirmed or might be modulators of mechanosensation rather than being directly involved in force transduction. A prerequisite for a candidate MS channel gene is to be found expressed in neurons displaying the purposed MS current. Therefore, we examined whether the expression of genes that have been proposed to encode excitatory MS channels in mammals correlates with the presence of a given MS current subtype across the scRNA-seq neurons (Figure 4A). As expected, *Piezo2* was detected in all neurons exhibiting the RA current. However, *Piezo2* was also detected in neurons for which no RA current could be extracted. *Tmem120a*, which has been proposed to sustain MS currents with slow kinetics in DRG neurons (Beaulieu-Laroche et al., 2020), was detected at high

level in all neuron types, including neurons lacking MS current. *Tmem150c* (Tentonin 3), which has been proposed to encode MS channels with slow kinetics in DRG and nodose ganglion neurons (Hong et al., 2016; Lu et al., 2020), was detected in most neurons, regardless of their mechanical signature. *Tmem87a*, a gene involved in melanoma adhesion/migration and sufficient to reconstitute MS currents in heterologous systems (Patkunarajah et al., 2020), was detected in some neurons, irrespective of the MS current subtypes. All three *Tmem63* genes that belong to an evolutionary conserved family of MS channel coding genes across eukaryotes (Murthy et al., 2018a) were differentially expressed. *Tmem63a* was detected in few neurons, but *Tmem63b* and *Tmem63c* were found in most MS

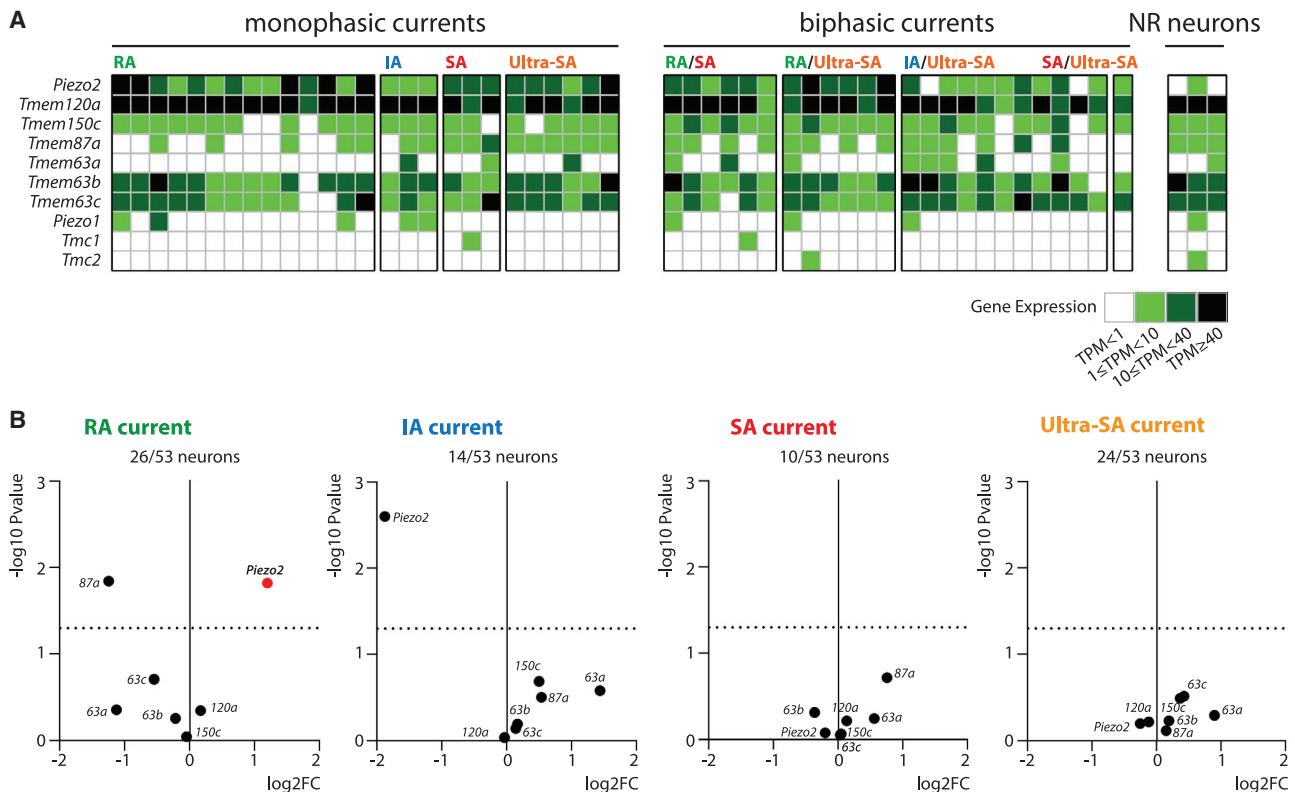


Figure 4. Expression analysis of genes proposed to encode MS channels

(A) Expression level of genes related to MS channel scRNA-seq neurons grouped by MS current type, as indicated. NR, non-responsive to mechanical stimulation.

(B) Differential expression plots of genes related to MS channels in neurons grouped by MS current type compared to neurons not expressing this current type, as specified. Dashed line represents p value of 0.05. For *Tmem* genes, only the label after *Tmem* is indicated for clarity.

current-expressing neurons. Finally, *Piezo1* was sporadically detected, while *Tmc1* and *Tmc2*, which contribute to the pore of MS channels in auditory and vestibular hair cells (Jia et al., 2020; Pan et al., 2018; Pan et al., 2013), were almost not expressed. Together, these results lend credence to the idea that PIEZO1 and TMC1 and 2 are unlikely to contribute to MS currents in DRG neurons. They also indicate that the other candidate genes are expressed in different MS current neuron families with no apparent clustering/specific expression.

Enrichment of transcripts as a means to identify MS channel gene candidates

The above data failed to reveal specific expression of a given MS channel gene in a particular neuronal group. Therefore, we assessed whether some transcripts showed statistically over-representation (e.g., enrichment) in neurons clustered by current types. We determined the differential expression of a gene by comparing its expression in neurons displaying a specific current type against the neurons that do not express this current type. The plots illustrated in Figure 4B provide graphical views of the enrichment of each MS channel gene in neurons with RA, IA, SA, and ultra-SA components. *Piezo2* is differentially expressed ($p = 0.015$) in neurons expressing RA currents, exhibiting a 2.3-fold enrichment. This result indicates that relative enrichment

rather than specific expression may be a pertinent criterion when selecting putative MS current genes. Remarkably, none of the other MS channel gene candidates were found to be differentially expressed ($p > 0.05$) in IA, SA, or ultra-SA MS current-expressing neurons. This lack of enrichment raises doubt about their possible contribution to specific MS currents in DRG neurons. As this result is intriguing regarding the recent literature, we set up proof-of-principle experiments to probe the functional relevance of *Tmem120a* and *Tmem150c* in MS currents.

Inhibition of *Tmem120a* expression does not alter DRG neuron MS currents

Our scRNA-seq data indicated that *Tmem120a* is broadly expressed in all neuron subclasses. We further characterized *Tmem120a* expression in DRG slices using the RNAscope *in situ* hybridization (ISH) technology coupled with immunostaining for the broader nociceptive and non-nociceptive markers, Peripherin and NF200, respectively (Goldstein et al., 1991; Padilla et al., 2007) (Figures 5A–5C; Figure S3). *Tmem120a* transcripts were detected in 75.0% of NF200-positive neurons and 67.4% of peripherin-positive DRG neurons (Figure 5B). Moreover, analysis of the cross-sectional area distribution revealed that *Tmem120a* mRNA was detected in the majority of DRG neurons over a large range of cell soma diameters (Figure 5C). Altogether,

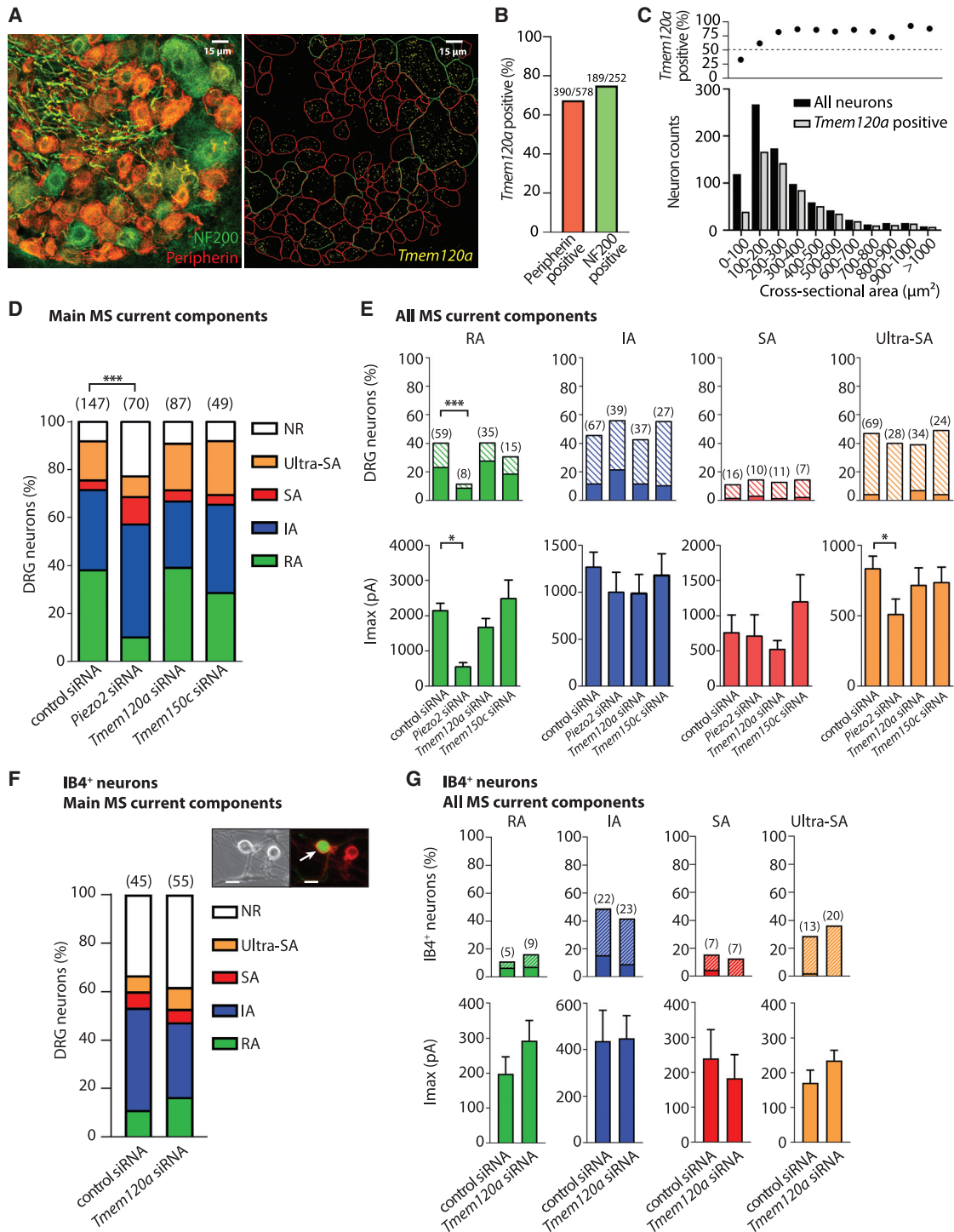


Figure 5. *Tmem120a* and *Tmem150c* do not contribute to DRG MS currents

(A) Representative images of fluorescent *in situ* hybridization for *Tmem120a* (right panel) in DRG neurons immuno-stained for peripherin and NF200 (left panel).

(B) Percentage of DRG neurons expressing *Tmem120a* mRNA in specified populations.

(C) Cross-sectional area distribution of *Tmem120a* mRNA-positive neurons. The top panel shows the percentage of *Tmem120a* positive neurons.

(D) Quantification of the prevalence of RA, IA, SA, and ultra-SA currents among DRG neurons electroporated with control, *Piezo2*, *Tmem120a*, or *Tmem150c* siRNAs. *** $p < 0.001$; χ^2 test.

(E) Prevalence of RA, IA, SA, and ultra-SA current components in siRNA-electroporated DRG neurons (top panels) and corresponding average maximal current amplitude (bottom panels). *** $p < 0.001$; * $p < 0.05$; χ^2 test (top panels) and Kruskal-Wallis multiple comparison (bottom panels).

(legend continued on next page)

these results confirm that *Tmem120a* is widely expressed in the different subpopulations of sensory neurons.

We performed small interfering RNA (siRNA) experiments in DRG neurons to determine whether *Tmem120a* could be responsible for a MS current. Since DRG neuron electroporation typically displays low transfection efficiency ($\approx 10\%$), we first assessed *Tmem120a* siRNA efficacy by qRT-PCR in NIH/3T3 electroporated cells (transfection efficiency 60%–80%), which constitutively express *Tmem120a* (Figure S4A). In these cells, *Tmem120a* siRNA transfection induced a decrease of $72\% \pm 5\%$ of *Tmem120a* mRNA level compared to non-targeting siRNA transfection (Figure S4D). Interestingly, knockdown of *Piezo1* but not *Tmem120a* inhibited the MS current present in NIH/3T3 cells (Figure S4F). The efficacy of siRNAs was confirmed in manually sorted electroporated DRG neurons by qRT-PCR showing about 90% decrease of transcript levels (Figure S4G).

Co-electroporation of siRNAs and GFP-plasmid was then performed in mouse DRG neurons, thereby allowing the fluorescent detection of transfected neurons. Non-targeting and *Piezo2* siRNAs were used as negative and positive controls, respectively. We first compared the proportions of DRG neurons classified according to their main MS current component. As previously reported (Coste et al., 2010), inhibition of *Piezo2* expression significantly ($p < 0.0001$, χ^2 test) altered the relative proportion of DRG neurons exhibiting the different MS currents, with notable decrease in the incidence of RA current-expressing neurons from 38.1% to 10.0% and consequential increase of non-responsive neurons from 8.2% to 22.9%. By contrast, inhibition of *Tmem120a* expression had no effect on the relative proportion of MS currents compared to control conditions ($p = 0.9$, χ^2 test) (Figure 5D). We next analyzed each MS current component quantified from mono- or bi-exponential fits of MS current recordings in siRNA-treated DRG neurons (Figure 5E). *Piezo2* siRNA treatment significantly reduced the proportion of neurons expressing the RA current component as well as the mean amplitude of the residual RA current. Once again, there were no significant changes in the proportion of any MS current components or in the mean amplitude of these components when *Tmem120a* expression was inhibited (Figure 5E).

To restrain the neuronal population investigated, we took advantage of the observation that TMEM120A protein immunostaining was detected in 80% of IB4⁺ DRG neurons (Beaulieu-Laroche et al., 2020). Therefore, we performed another set of experiments by selectively recording from IB4⁺ neurons identified using IB4-Alexa Fluor 568 conjugate staining. Consistent with our previous results, we found no differences regarding either the incidence or the amplitude of the different MS current components between *Tmem120a* and non-targeting siRNA-treated neurons (Figures 5F and 5G). Furthermore, we cloned *Tmem120a* cDNA from mouse DRG into an expression vector.

Cell-poking and pressure-clamp experiments showed that *Tmem120a* overexpression did not induce MS currents in HEK-P1KO cells in which *PIEZO1* has been deleted (Dubin et al., 2017) (Figure S5). Altogether, these data suggest that *Tmem120a* does not contribute to any MS currents in DRG neurons.

Inhibition of *Tmem150c* expression does not impair MS currents in DRG neurons

Tmem150c has been proposed to encode SA MS channels in proprioceptive DRG neurons contributing to motor coordination (Hong et al., 2016). This conclusion has been challenged by independent groups, because *Tmem150c* expression by itself does not appear to generate MS current but rather modulates the activity of mechano-gated channels including PIEZO1, PIEZO2, and the two-pore domain K⁺ channel TREK1 (Anderson et al., 2018; Dubin et al., 2017). Our scRNA-seq data indicated that *Tmem150c* is not enriched in a particular subset of DRG neurons. Therefore, to gain more understanding about its role in MS current generation, we recorded from *Tmem150c* siRNA electroporated DRG neurons. We found no differences whatsoever regarding either the incidence or the amplitude of the different MS current components in *Tmem150c* siRNA-treated neurons compared with non-targeting siRNA-treated neurons (Figures 5D and 5E). These data argue against a role of *Tmem150c* in sustaining a particular type of MS current in DRG neurons.

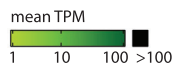
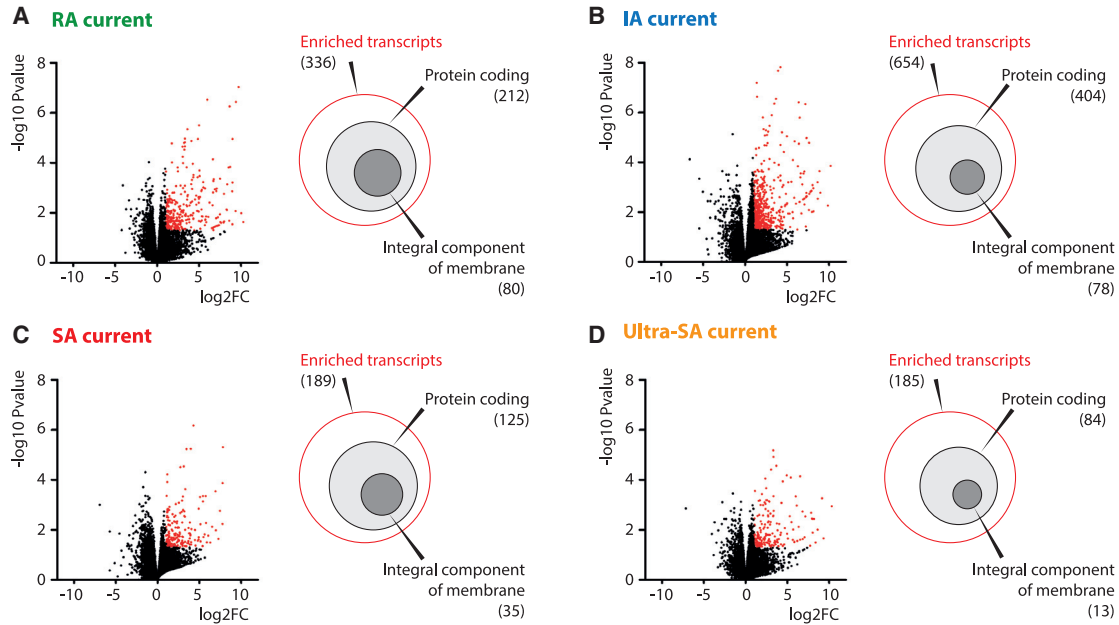
Genes associated with DRG MS current types

Enrichment of *Piezo2* in the subset of RA current expressing neurons provides a rationale to identify candidate genes coding for or regulating MS channels. Therefore, we looked for transcripts differentially expressed ($p < 0.05$) and enriched at least 2-fold in neurons grouped by MS current type (Figures 6A–6D). We provide a list of transcripts associated with RA, IA, SA, and ultra-SA currents containing 212, 404, 125, and 84 protein coding genes, respectively (Table S2). As can be seen in Figure 6E, *Piezo2* emerged in the top 15% of most expressed genes among the enriched ones. Therefore, we reasoned that both enrichment and mRNA abundance in the corresponding neuronal population may be good criteria to pinpoint molecular determinants associated with MS current phenotype. Additionally, gene ontology (GO) analysis was used to annotate these genes with relevant knowledge such as detection of a mechanical stimulus, ion channel activity, and integral component of the membrane. The top 40 of the most expressed genes associated with MS current type are listed in Figure 6E. Among those, *Piezo2* is the only gene known to encode a protein with demonstrated function in mechanical transduction. Moreover, the few genes known to encode ion channels, such as *Scn10a* encoding the voltage

(F) Stacked histogram showing the prevalence of RA, IA, SA, and ultra-SA currents in IB4-positive neurons electroporated with control or *Tmem120a* siRNAs. χ^2 test shows no statistical difference. Inset: arrow shows a DRG neuron positive for IB4 (red) and siRNA transfection (green). Scale bar, 10 μ m.

(G) Prevalence of RA, IA, SA, and ultra-SA current components in siRNA-electroporated IB4-positive neurons (top panels) and corresponding average maximal current amplitude (bottom panels). Mann-Whitney test shows no statistical difference.

For panels (D) and (F), neurons responding with biphasic MS currents were classified according to the MS current type contributing the most. NR, non-responders. For (E) and (G) top panels, solid and striped colors indicate neurons with monophasic or biphasic MS currents, respectively. For all panels, n numbers are indicated in brackets, and 3–6 mice were used for each siRNA condition. Error bars represent SEM.



- Biological process : detection of mechanical stimulus (GO:0050982)
- Molecular function : ion channel activity (GO:0005216)
- Cellular component : integral component of membrane (GO:0016021)

(legend on next page)

activated sodium channel Nav1.8 (Han et al., 2016), are well characterized and unlikely to encode MS channels. Several genes are known to code for proteins inserted in the membrane, a feature common to ion channels. However, as GO resource reflects our current biological knowledge many of these candidate genes remain to be functionally characterized. By refining from 13,000 transcripts expressed per DRG neuron to only hundreds of candidates, this dataset represents a valuable resource for the identification of genes involved in the generation of DRG MS currents.

DISCUSSION

Patch-clamping of cultured DRG neurons is compatible with scRNA-seq classification

Direct relationship between mechanosensory properties and molecular phenotypes of DRG neurons determined by whole-transcriptome analysis has never been explored. To identify molecular features associated with specific mechanosensory functions and phenotypes, we have combined scRNA-seq profiling with electrophysiological recordings of individual DRG neurons. We provided full transcriptome data from single neurons in culture after characterization of MS currents, which were classified based on their inactivation kinetics. Coupling patch-clamp recording with mechanical stimulation required the use of adhering cultured DRG neurons. This approach is labor intensive and low throughput and differs somehow from previous scRNA-seq classification studies for which DRG neurons were collected shortly after ganglionic dissociation (Li et al., 2016; Sharma et al., 2020; Usoskin et al., 2015; Zeisel et al., 2018). Yet, 85% of the processed mRNA samples met quality standards for RNA-seq. The molecular classification of our small and heterogeneous group of DRG neurons, however, was challenging because of the resulting low statistical power. Advances in microfluidics for single-cell partitioning have enabled scRNA-seq studies performed on samples of over 1,000 cells, subdividing DRG neurons into a total of up to 17 transcriptional clusters (Sharma et al., 2020; Zeisel et al., 2018). To achieve high-quality classification of our neuron sample, we combined our single-cell transcriptomes with the larger single-DRG neuron dataset from Zeisel and collaborators (Zeisel et al., 2018). Therefore, despite its modest size, we succeeded to map all the neurons from our sample into DRG neuron transcriptional clusters. They are distributed among 11 of the 17 transcriptional clusters corresponding to 7 of the 8 main classes of neurons. The clusters that are not represented are PSNF2 (from NF neurons), PSNP2 (from NP1 neurons), PSPEP4 (from PEP1 neurons), and the three clusters PSPEP6-8, which together constitute the TrpM8 population. The absence of TrpM8 neurons in our sample is consistent with their lack of role in mechanosensation (Knowlton et al., 2013). It is possible that PSNP2 and PSPEP4 constitute subgroups of NP1 and PEP1 neurons that are not MS, but our rela-

tively small sample of neurons does not allow a definite conclusion. However, the absence of PSNF2 neurons, thought to represent a cluster of proprioceptors (Usoskin et al., 2015), likely stems from an undersized sample. Yet, our results attest that the culture of neurons, coupled to patch-clamp recording, does not prevent their classification and offers an extensive view of the main populations of DRG MS neurons. Thus, patch-clamp recording of MS currents is compatible with the production of a quantitative dataset that resolves mRNAs for all known genes in single mechanosensory neurons.

Distribution of MS current types in transcriptionally defined neurons

The distribution of MS currents in DRG neurons has been addressed over the past by distinguishing neuronal subsets using morphological and electrophysiological parameters as well as IB4 staining (Coste et al., 2007; Drew et al., 2002, 2004; Hu and Lewin, 2006; Lechner and Lewin, 2009; Prato et al., 2017). These approaches led to the view that large diameter, non-nociceptive neurons express mainly RA MS currents, whereas medium- and small-diameter nociceptors express MS currents with slower kinetics. Subsets of DRG neurons labeled *in vivo* using genetically modified mice confirmed the tendency of proprioceptors and non-nociceptive A-type LTMRs to express RA MS currents (Woo et al., 2015; Zheng et al., 2019) and showed that C-LTMRs express MS currents with rapid and/or slow kinetics (Delfini et al., 2013; Lou et al., 2013). The accurate characterization of four distinct types of DRG MS currents in classified neurons using scRNA-seq enabled to study their distribution in DRG neuron subsets.

Our results showed that the RA MS current is the main subtype in NF neuronal population, in line with the remarkable phenotype of *Piezo2* KO animals related to innocuous touch and proprioception (Florez-Paz et al., 2016; Ranade et al., 2014b; Woo et al., 2015).

Consistent with *Piezo2* modest contribution to mechanical nociception (Murthy et al., 2018b), RA current type contributes to a lesser extent to MS currents in NP1, PEP1, and PEP2 neuronal subpopulations. The PEP1 neurons express predominantly the IA MS current type. This suggests that IA MS current may be the main transducer of noxious mechanical stimuli in C-type peptidergic nociceptors. The contribution of SA and ultra-SA currents in these neurons seems minimal. Interestingly, the opposite is true in PEP2 neurons, in which ultra-SA current type contributes the most, whereas IA current type is almost absent. This suggests that A δ -nociceptors and C-type peptidergic nociceptors use distinct sets of MS ion channels for mechanical pain detection. These differences could contribute to the signaling of distinct mechanosensory modalities by PEP1 and PEP2 nociceptors.

Importantly, RA current type is the main contributor of MS currents in NP2 neurons. These neurons, which have been shown to respond to mechanical stimulus, heat, and a large array of pruritogens, mediate itch behavior but not pain (Han et al., 2013).

Figure 6. Potential molecular determinants of DRG MS channels

(A–D) Left panels: volcano plots of transcripts expressed in neurons grouped by specific MS current type compared to neurons not expressing this current type, as indicated. Red dots illustrate transcripts significantly enriched, the full list of which is available in Table S2. Right panels: Euler diagrams showing among the enriched transcripts those that code for proteins (light gray) and those that code for integral membrane proteins (dark gray).

(E) Lists of the top-40 most-expressed protein-coding genes among enriched transcripts in DRG neurons grouped by MS current type.

Therefore, these results suggest that *Piezo2* actively contributes to itch sensing, by opposition to its expression in Merkel cells in which *Piezo2* inhibition produces allodynia, a pathological itch sensation produced by innocuous touch (Feng et al., 2018).

An elegant study by Von Buchholtz and colleagues mapped mechanosensory functions to transcriptomic classes by combining *in vivo* calcium imaging and multiplexed ISH (von Buchholtz et al., 2021). Notably, complete loss of A β LTMR responses and loss of C-LTMRs responses to gentle but not noxious stimulations are seen in *Piezo2*-deleted mice. Although this study was performed on trigeminal ganglion neurons, which differ notably from DRG neurons (Lopes et al., 2017; Megat et al., 2019; Price and Flores, 2007), our results are consistent with these observations. Indeed, we detected almost only RA currents in NF neurons related to A β LTMR, whereas both RA and ultra-SA currents are expressed in C-LTMR-related TH neurons. This suggests that the detection of high-threshold mechanical stimulus in C-LTMRs is mediated by ultra-SA currents.

No evidence for *Tmem120a* and *Tmem150c* in sustaining slow MS currents

While a compelling body of evidence indicates that *Piezo2* generates RA-type MS current in DRG neurons, the molecular identity of genes coding for slow MS currents has remained elusive (Delmas and Coste, 2013; Ranade et al., 2015). Recently, new gene candidates have been proposed to encode slow-type MS currents in DRG neurons. *Tmem120a* has been suggested to be expressed in small- to medium-diameter neurons and to mediate the ultra-slowly adapting MS current (Beaulieu-Laroche et al., 2020). Our results do not support this conclusion. First, our single-cell transcriptome analysis indicates that *Tmem120a* expression is not restricted to nociceptors and is not enriched in slowly or ultra-slowly adapting MS current-expressing neurons. This is consistent with our analysis of the cross-sectional area distribution of *Tmem120a*-positive DRG neurons in *ISH* experiments. When normalized to the overall population, *Tmem120a* was detected in all subtypes of DRG neuron cell-body diameters, including the largest ones expressing NF200. Nevertheless, the possibility that *Tmem120* contributes to MS currents without being selectively expressed/enriched in a particular population was still open. However, our *Tmem120a* siRNA experiments performed either on the whole DRG neuron population or restricted to IB4⁺ neurons showed no changes in the proportion of slowly or ultra-slowly MS current-expressing neurons, nor in the mean amplitude of these current components. Our siRNA assays benefited from our extensive kinetics classification of MS currents and from the inclusion of a *piezo2* siRNA effective target knockdown. Thus, the broad expression of *Tmem120a* in DRG neurons, along with the lack of appreciable effects of *Tmem120a* siRNA treatment on endogenous MS currents, cast doubt about its role in mediating SA/ultra-SA MS currents. Moreover, overexpression of mouse *Tmem120a* in heterologous system did not induce MS channel activity. However, our data do not question *Tmem120a* involvement in pain sensing, which has been shown recently in inflammatory, but not neuropathic, mechanical hyperalgesia in rats (Bonet et al., 2021). The molecular function of *Tmem120a* needs to be clarified in future work.

Tmem150c has been proposed to encode slowly adapting MS channels in DRG proprioceptive neurons (Hong et al., 2016), but this inference has been challenged. Indeed, we and others have shown that, contrary to what was initially reported, *Tmem150c* expression in heterologous system does not induce MS currents by itself (Anderson et al., 2018; Dubin et al., 2017) but instead modulates the properties of MS ion channels when co-expressed (Anderson et al., 2018). In addition, no slowly adapting current type was detected in proprioceptive neurons labeled *in vivo* using genetically modified mice (Woo et al., 2015). *Tmem150c* was found to be broadly expressed in our single-cell transcriptome analysis, and our siRNA experiments showed that *Tmem150c* knockdown caused no changes in the proportion or amplitude of any MS currents, suggesting that *Tmem150c* is not a prime contributor to MS currents in DRG neurons. To note, *Tmem150c* has been proposed recently to contribute to slowly adapting MS currents in nodose ganglion baroreceptors (Lu et al., 2020). Future studies will help resolve these controversies.

Molecular bases of the kinetically distinct MS current subtypes in DRG

Intensive efforts have been deployed to identify mammalian MS channels for decades, since the earliest indications of their existence in auditory hair cells (Corey and Hudspeth, 1979). Identifying MS channel genes represents a crucial challenge for the field of nociception and may have many clinical implications in acute as well as inflammatory and chronic pain. In addition, it would be potentially relevant beyond somatosensation as exemplified by PIEZO channel implication in many physiological functions and diseases in humans (Ma et al., 2018, 2021; Marshall et al., 2020; McMillin et al., 2014). Therefore, by correlating DRG MS current properties with co-expressed genes at the single-cell level, our study provides a valuable resource for identifying new molecular entities involved in mechanotransduction.

Our extensive characterization of MS current properties from large neuronal samples showed that 4 distinct types of MS currents are present in mouse DRG neurons. It is now well established that *Piezo2* encodes MS channels responsible for RA currents. Does *Piezo2* contribute to other types of MS currents? It has been shown that overexpression of *Tmem150c* with *Piezo2* in heterologous systems induces slowing of PIEZO2 current inactivation to values close to IA current type (Anderson et al., 2018). However, *Piezo2* deletion or knockdown studies in DRG neurons, including this work, have shown no alteration of IA currents (Coste et al., 2010; Ranade et al., 2014b), and a possible compensatory increase in IA current responses has been reported in proprioceptors (Woo et al., 2015). This suggests that *Piezo2* does not encode MS channels responsible for IA currents in DRG neurons. The situation differs in trigeminal corneal neurons where a non-specific decrease of currents with intermediate and slow kinetics has been reported in *Piezo2* KO mice (Fernández-Trillo et al., 2020). We also observed a modest effect of *Piezo2* inhibition on the amplitude of ultra-SA currents. It cannot be excluded that this decrease is due to a RA current component masked in neurons with large ultra-SA currents. However, this modest impairment is still observable when current amplitude was measured at the end of the mechanical stimulus, i.e., when RA currents are expected to be fully inactivated (data not shown). Inhibition of a

Piezo2 splice variant could be responsible for this effect, as *Piezo2* extensive alternative splicing affecting inactivation kinetics has been reported in DRG neurons, although *Piezo2* splicing variants displayed inactivation kinetics still in the range of RA current subtype (Szczoł et al., 2017). In any case, this effect is slight and does not alter the proportion of neurons expressing the ultra-SA current, arguing that the primary contributor of ultra-SA currents is distinct from PIEZO2.

Notwithstanding, the nature of the molecular entities involved in IA, SA, and ultra SA currents remains unknown. In addition, the question of whether these currents are generated by multiple or single-molecular entities is not yet resolved. Indeed, proximate environment such as membrane composition, attachment to extracellular matrix or subcortical cytoskeleton organization can potentially modify membrane bilayer tension and inserted MS channels properties including kinetics (Cox et al., 2016; Del Mármol et al., 2018; Syeda et al., 2016; Teng et al., 2015). In this scenario, accessory subunits conferring distinct inactivation properties to a unique MS channel could be encoded by genes found to be enriched in a subset of DRG neurons.

Evidence suggests that the different currents are sustained by molecularly distinct ion channels. Indeed, three types of cationic MS ion channels with sustained activity but distinguishable from their unitary conductance have been described in DRG neurons (Cho et al., 2002, 2006). Moreover, ultra-SA currents are blocked selectively by the conopeptide NMB1 (Drew et al., 2007), suggesting that this current is sustained by a specific pool of MS channels. Hence, several MS channel coding genes remain to be discovered in DRG neurons. By identifying the genes enriched in DRG neurons with distinct mechanical phenotypes, our study lays the foundations for the identification of their molecular entities. Testing these candidates using siRNA experiments coupled with patch-clamp recording in DRG neurons may identify genes involved in mechanosensation. Importantly, given the broad involvement of mechanotransduction in physiological functions and the dynamism of the mechanobiology field, illustrated by the development of novel mechanobiology assays (Kurth et al., 2012; Xu et al., 2018), our data could also be used to identify mechanosensors or associated proteins in other biological tissues.

Limitations of the study

Transcriptomics data were generated from DRG neurons cultured *in vitro*. This should be considered when comparing these data to those obtained in native state, as these conditions can potentially alter the gene-expression profile of cells and reduce cellular heterogeneity of the donor tissue. Performing Patch-seq experiments in DRG tissue slices could circumvent this limitation.

STAR★METHODS

Detailed methods are provided in the online version of this paper and include the following:

- KEY RESOURCES TABLE
- RESOURCE AVAILABILITY
 - Lead contact

- Materials availability
- Data and code availability
- EXPERIMENTAL MODEL AND SUBJECT DETAILS
 - Animals
 - Dorsal root ganglion neuron culture
 - Cell lines
- METHOD DETAILS
 - Electrophysiology
 - Mechanical stimulation
 - Pressure-clamp experiments
 - Single-cell library preparation
 - Processing, quality control and filtering of single-cell RNA-seq data
 - Dorsal root ganglion neuron clustering
 - Electroporation
 - Molecular cloning of Tmem120a
 - Transfection of HEK-P1KO cells
 - qRT-PCR experiments
 - *In Situ* Hybridization experiments
 - Immunofluorescence staining
 - Gene Ontology (GO)
- QUANTIFICATION AND STATISTICAL ANALYSIS
 - Mechanosensitive current analysis
 - Differential expression analysis
 - qPCR Analysis
 - Image Acquisition and Analysis
- STATISTICAL ANALYSIS

SUPPLEMENTAL INFORMATION

Supplemental information can be found online at <https://doi.org/10.1016/j.celrep.2021.109914>.

ACKNOWLEDGMENTS

This project has received funding from the European Research Council (ERC) under the European Union's Horizon 2020 research and innovation programme (Grant agreement No. 678610). RNA sequencing was done by Proflexpert, "Génomique & Microgénomique" service, Lyon, FRANCE. We thank Virginie Penalba and Axel Fernandez for expert technical assistance and Dr. Nancy Osorio, Dr. Françoise Padilla, and Dr. Nicolas Grillet for critical reading of the manuscript.

AUTHOR CONTRIBUTIONS

L.B. and B.C. recorded and collected DRG neurons for RNA sequencing. N.S. and Y.M. prepared sequencing libraries. T.P. conducted all bioinformatics analysis. N.S. performed RNAscope experiments. A.L. and N.S. conducted qPCR experiments. T.P. and L.B. conducted siRNA electrophysiological experiments. B.C. conceived and supervised all aspects of the project. T.P. and B.C. prepared the figures and T.P., P.D., and B.C. wrote the manuscript with input from L.B.

DECLARATION OF INTERESTS

The authors declare no competing interests.

Received: April 26, 2021
 Revised: July 16, 2021
 Accepted: October 9, 2021
 Published: November 2, 2021

REFERENCES

- Abraira, V.E., and Ginty, D.D. (2013). The sensory neurons of touch. *Neuron* 79, 618–639.
- Anderson, E.O., Schneider, E.R., Matson, J.D., Gracheva, E.O., and Bagriantsev, S.N. (2018). TMEM150C/Tentonin3 Is a Regulator of Mechano-gated Ion Channels. *Cell Rep.* 23, 701–708.
- Ashburner, M., Ball, C.A., Blake, J.A., Botstein, D., Butler, H., Cherry, J.M., Davis, A.P., Dolinski, K., Dwight, S.S., Eppig, J.T., et al.; The Gene Ontology Consortium (2000). Gene ontology: tool for the unification of biology. *Nat. Genet.* 25, 25–29.
- Basbaum, A.I., Bautista, D.M., Scherrer, G., and Julius, D. (2009). Cellular and molecular mechanisms of pain. *Cell* 139, 267–284.
- Beaulieu-Laroche, L., Christin, M., Donoghue, A., Agosti, F., Yousefpour, N., Petitjean, H., Davidova, A., Stanton, C., Khan, U., Dietz, C., et al. (2020). TACAN Is an Ion Channel Involved in Sensing Mechanical Pain. *Cell* 180, 956–967.
- Bonet, I.J.M., Araldi, D., Bogen, O., and Levine, J.D. (2021). Involvement of TACAN, a Mechanotransducing Ion Channel, in Inflammatory But Not Neuropathic Hyperalgesia in the Rat. *J. Pain* 22, 498–508.
- Cadwell, C.R., Palasantza, A., Jiang, X., Berens, P., Deng, Q., Yilmaz, M., Reimer, J., Shen, S., Bethge, M., Tolia, K.F., et al. (2016). Electrophysiological, transcriptomic and morphologic profiling of single neurons using Patch-seq. *Nat. Biotechnol.* 34, 199–203.
- Cain, D.M., Khasabov, S.G., and Simone, D.A. (2001). Response properties of mechanoreceptors and nociceptors in mouse glabrous skin: an in vivo study. *J. Neurophysiol.* 85, 1561–1574.
- Case, L.K., Lijencrantz, J., Madian, N., Necaie, A., Tubbs, J., McCall, M., Bradson, M.L., Szczot, M., Pitcher, M.H., Ghitani, N., et al. (2021). Innocuous pressure sensation requires A-type afferents but not functional PIEZO2 channels in humans. *Nat. Commun.* 12, 657.
- Cavanaugh, D.J., Lee, H., Lo, L., Shields, S.D., Zylka, M.J., Basbaum, A.I., and Anderson, D.J. (2009). Distinct subsets of unmyelinated primary sensory fibers mediate behavioral responses to noxious thermal and mechanical stimuli. *Proc. Natl. Acad. Sci. USA* 106, 9075–9080.
- Chesler, A.T., Szczot, M., Bharucha-Goebel, D., Ćeko, M., Donkervoort, S., Laubacher, C., Hayes, L.H., Alter, K., Zampieri, C., Stanley, C., et al. (2016). The Role of PIEZO2 in Human Mechanosensation. *N. Engl. J. Med.* 375, 1355–1364.
- Cho, H., Shin, J., Shin, C.Y., Lee, S.Y., and Oh, U. (2002). Mechanosensitive ion channels in cultured sensory neurons of neonatal rats. *J. Neurosci.* 22, 1238–1247.
- Cho, H., Koo, J.Y., Kim, S., Park, S.P., Yang, Y., and Oh, U. (2006). A novel mechanosensitive channel identified in sensory neurons. *Eur. J. Neurosci.* 23, 2543–2550.
- Corey, D.P., and Hudspeth, A.J. (1979). Response latency of vertebrate hair cells. *Biophys. J.* 26, 499–506.
- Corey, D.P., Akyuz, N., and Holt, J.R. (2019). Function and Dysfunction of TMC Channels in Inner Ear Hair Cells. *Cold Spring Harb. Perspect. Med.* 9, a033506.
- Coste, B., Crest, M., and Delmas, P. (2007). Pharmacological dissection and distribution of Na^v1.9, T-type Ca²⁺ currents, and mechanically activated cation currents in different populations of DRG neurons. *J. Gen. Physiol.* 129, 57–77.
- Coste, B., Mathur, J., Schmidt, M., Earley, T.J., Ranade, S., Petrus, M.J., Dubin, A.E., and Patapoutian, A. (2010). Piezo1 and Piezo2 are essential components of distinct mechanically activated cation channels. *Science* 330, 55–60.
- Coste, B., Xiao, B., Santos, J.S., Syeda, R., Grandl, J., Spencer, K.S., Kim, S.E., Schmidt, M., Mathur, J., Dubin, A.E., et al. (2012). Piezo proteins are pore-forming subunits of mechanically activated channels. *Nature* 483, 176–181.
- Cox, C.D., Bae, C., Ziegler, L., Hartley, S., Nikolova-Krstevski, V., Rohde, P.R., Ng, C.A., Sachs, F., Gottlieb, P.A., and Martinac, B. (2016). Removal of the mechanoprotective influence of the cytoskeleton reveals PIEZO1 is gated by bilayer tension. *Nat. Commun.* 7, 10366.
- Del Mármol, J.I., Touhara, K.K., Croft, G., and MacKinnon, R. (2018). Piezo1 forms a slowly-inactivating mechanosensory channel in mouse embryonic stem cells. *eLife* 7, e33149.
- Delfini, M.C., Mantilleri, A., Gaillard, S., Hao, J., Reynders, A., Malapert, P., Alonso, S., François, A., Barrere, C., Seal, R., et al. (2013). TFAA4, a chemokine-like protein, modulates injury-induced mechanical and chemical pain hypersensitivity in mice. *Cell Rep.* 5, 378–388.
- Delmas, P., and Coste, B. (2013). Mechano-gated ion channels in sensory systems. *Cell* 155, 278–284.
- Drew, L.J., Wood, J.N., and Cesare, P. (2002). Distinct mechanosensitive properties of capsaicin-sensitive and -insensitive sensory neurons. *J. Neurosci.* 22, RC228.
- Dong, X., and Dong, X. (2018). Peripheral and Central Mechanisms of Itch. *Neuron* 98, 482–494.
- Drew, L.J., Rohrer, D.K., Price, M.P., Blaver, K.E., Cockayne, D.A., Cesare, P., and Wood, J.N. (2004). Acid-sensing ion channels ASIC2 and ASIC3 do not contribute to mechanically activated currents in mammalian sensory neurons. *J. Physiol.* 556, 691–710.
- Drew, L.J., Rugiero, F., Cesare, P., Gale, J.E., Abrahamsen, B., Bowden, S., Heinzmann, S., Robinson, M., Brust, A., Colless, B., et al. (2007). High-threshold mechanosensitive ion channels blocked by a novel conopeptide mediate pressure-evoked pain. *PLoS ONE* 2, e515.
- Dubin, A.E., Murthy, S., Lewis, A.H., Brosse, L., Cahalan, S.M., Grandl, J., Coste, B., and Patapoutian, A. (2017). Endogenous Piezo1 Can Confound Mechanically Activated Channel Identification and Characterization. *Neuron* 94, 266–270.
- Feng, J., Luo, J., Yang, P., Du, J., Kim, B.S., and Hu, H. (2018). Piezo2 channel-Merkel cell signaling modulates the conversion of touch to itch. *Science* 360, 530–533.
- Fernández-Trillo, J., Florez-Paz, D., Íñigo-Portugués, A., González-González, O., Del Campo, A.G., González, A., Viana, F., Belmonte, C., and Gomis, A. (2020). Piezo2 Mediates Low-Threshold Mechanically Evoked Pain in the Cornea. *J. Neurosci.* 40, 8976–8993.
- Florez-Paz, D., Bali, K.K., Kuner, R., and Gomis, A. (2016). A critical role for Piezo2 channels in the mechanotransduction of mouse proprioceptive neurons. *Sci. Rep.* 6, 25923.
- Francois, A., Schuetter, N., Laffray, S., Sanguesa, J., Pizzoccaro, A., Dubel, S., Mantilleri, A., Nargeot, J., Noel, J., Wood, J.N., et al. (2015). The Low-Threshold Calcium Channel Cav3.2 Determines Low-Threshold Mechanoreceptor Function. *Cell Rep.* 10, 370–382.
- Fuzik, J., Zeisel, A., Máté, Z., Calvigioni, D., Yanagawa, Y., Szabó, G., Linnarsson, S., and Harkany, T. (2016). Integration of electrophysiological recordings with single-cell RNA-seq data identifies neuronal subtypes. *Nat. Biotechnol.* 34, 175–183.
- Gene Ontology, C.; Gene Ontology Consortium (2021). The Gene Ontology resource: enriching a GOld mine. *Nucleic Acids Res.* 49 (D1), D325–D334.
- Goldstein, M.E., House, S.B., and Gainer, H. (1991). NF-L and peripherin immunoreactivities define distinct classes of rat sensory ganglion cells. *J. Neurosci. Res.* 30, 92–104.
- Haghverdi, L., Lun, A.T.L., Morgan, M.D., and Marioni, J.C. (2018). Batch effects in single-cell RNA-sequencing data are corrected by matching mutual nearest neighbors. *Nat. Biotechnol.* 36, 421–427.
- Han, L., Ma, C., Liu, Q., Weng, H.J., Cui, Y., Tang, Z., Kim, Y., Nie, H., Qu, L., Patel, K.N., et al. (2013). A subpopulation of nociceptors specifically linked to itch. *Nat. Neurosci.* 16, 174–182.
- Han, C., Huang, J., and Waxman, S.G. (2016). Sodium channel Nav1.8: Emerging links to human disease. *Neurology* 86, 473–483.
- Hao, J., and Delmas, P. (2010). Multiple desensitization mechanisms of mechanotransducer channels shape firing of mechanosensory neurons. *J. Neurosci.* 30, 13384–13395.

- Hong, G.S., Lee, B., Wee, J., Chun, H., Kim, H., Jung, J., Cha, J.Y., Riew, T.R., Kim, G.H., Kim, I.B., and Oh, U. (2016). Tentonin 3/TMEM150c Confers Distinct Mechanosensitive Currents in Dorsal-Root Ganglion Neurons with Proprioceptive Function. *Neuron* *91*, 708–710.
- Hu, J., and Lewin, G.R. (2006). Mechanosensitive currents in the neurites of cultured mouse sensory neurones. *J. Physiol.* *577*, 815–828.
- Jia, Y., Zhao, Y., Kusakizako, T., Wang, Y., Pan, C., Zhang, Y., Nureki, O., Hattori, M., and Yan, Z. (2020). TMC1 and TMC2 Proteins Are Pore-Forming Subunits of Mechanosensitive Ion Channels. *Neuron* *105*, 310–321.
- Kefauver, J.M., Ward, A.B., and Patapoutian, A. (2020). Discoveries in structure and physiology of mechanically activated ion channels. *Nature* *587*, 567–576.
- Knowlton, W.M., Palkar, R., Lippoldt, E.K., McCoy, D.D., Baluch, F., Chen, J., and McKemy, D.D. (2013). A sensory-labeled line for cold: TRPM8-expressing sensory neurons define the cellular basis for cold, cold pain, and cooling-mediated analgesia. *J. Neurosci.* *33*, 2837–2848.
- Koltzenburg, M., Stucky, C.L., and Lewin, G.R. (1997). Receptive properties of mouse sensory neurons innervating hairy skin. *J. Neurophysiol.* *78*, 1841–1850.
- Kurth, F., Eyer, K., Franco-Obregón, A., and Dittrich, P.S. (2012). A new mechanobiological era: microfluidic pathways to apply and sense forces at the cellular level. *Curr. Opin. Chem. Biol.* *16*, 400–408.
- Lawrence, M., Huber, W., Pagès, H., Aboyoun, P., Carlson, M., Gentleman, R., Morgan, M.T., and Carey, V.J. (2013). Software for computing and annotating genomic ranges. *PLoS Comput. Biol.* *9*, e1003118.
- Lechner, S.G., and Lewin, G.R. (2009). Peripheral sensitisation of nociceptors via G-protein-dependent potentiation of mechanotransduction currents. *J. Physiol.* *587*, 3493–3503.
- Li, L., Rutlin, M., Abirra, V.E., Cassidy, C., Kus, L., Gong, S., Jankowski, M.P., Luo, W., Heintz, N., Koerber, H.R., et al. (2011). The functional organization of cutaneous low-threshold mechanosensory neurons. *Cell* *147*, 1615–1627.
- Li, C.L., Li, K.C., Wu, D., Chen, Y., Luo, H., Zhao, J.R., Wang, S.S., Sun, M.M., Lu, Y.J., Zhong, Y.Q., et al. (2016). Somatosensory neuron types identified by high-coverage single-cell RNA-sequencing and functional heterogeneity. *Cell Res.* *26*, 83–102.
- Lopes, D.M., Denk, F., and McMahon, S.B. (2017). The Molecular Fingerprint of Dorsal Root and Trigeminal Ganglion Neurons. *Front. Mol. Neurosci.* *10*, 304.
- Lou, S., Duan, B., Vong, L., Lowell, B.B., and Ma, Q. (2013). Runx1 controls terminal morphology and mechanosensitivity of VGLUT3-expressing C-mechanoreceptors. *J. Neurosci.* *33*, 870–882.
- Lu, H.J., Nguyen, T.L., Hong, G.S., Pak, S., Kim, H., Kim, H., Kim, D.Y., Kim, S.Y., Shen, Y., Ryu, P.D., et al. (2020). Tentonin 3/TMEM150C senses blood pressure changes in the aortic arch. *J. Clin. Invest.* *130*, 3671–3683.
- Ma, S., Cahalan, S., LaMonte, G., Grubaugh, N.D., Zeng, W., Murthy, S.E., Paytas, E., Gamin, R., Lukacs, V., Whitwam, T., et al. (2018). Common PIEZO1 Allele in African Populations Causes RBC Dehydration and Attenuates Plasmodium Infection. *Cell* *173*, 443–455.
- Ma, S., Dubin, A.E., Zhang, Y., Mousavi, S.A.R., Wang, Y., Coombs, A.M., Loud, M., Andolfo, I., and Patapoutian, A. (2021). A role of PIEZO1 in iron metabolism in mice and humans. *Cell* *184*, 969–982.
- Marshall, K.L., Saade, D., Ghitani, N., Coombs, A.M., Szczot, M., Keller, J., Ogata, T., Daou, I., Stowers, L.T., Bönnemann, C.G., et al. (2020). PIEZO2 in sensory neurons and urothelial cells coordinates urination. *Nature* *588*, 290–295.
- Martin, M. (2011). Cutadapt removes adapter sequences from high-throughput sequencing reads. *EMBnet. J.* *17*, 10–12.
- McCarter, G.C., Reichling, D.B., and Levine, J.D. (1999). Mechanical transduction by rat dorsal root ganglion neurons in vitro. *Neurosci. Lett.* *273*, 179–182.
- McMillin, M.J., Beck, A.E., Chong, J.X., Shively, K.M., Buckingham, K.J., Gildersleeve, H.I., Aracena, M.I., Aylsworth, A.S., Bitoun, P., Carey, J.C., et al.; University of Washington Center for Mendelian Genomics (2014). Mutations in PIEZO2 cause Gordon syndrome, Marden-Walker syndrome, and distal arthrogyriposis type 5. *Am. J. Hum. Genet.* *94*, 734–744.
- Megat, S., Ray, P.R., Tavares-Ferreira, D., Moy, J.K., Sankaranarayanan, I., Wangzhou, A., Fang Lou, T., Barragan-Iglesias, P., Campbell, Z.T., Dussor, G., and Price, T.J. (2019). Differences between Dorsal Root and Trigeminal Ganglion Nociceptors in Mice Revealed by Translational Profiling. *J. Neurosci.* *39*, 6829–6847.
- Michel, N., Narayanan, P., Shomroni, O., and Schmidt, M. (2020). Maturation Changes in Mouse Cutaneous Touch and Piezo2-Mediated Mechanotransduction. *Cell Rep.* *32*, 107912.
- Min, S., Chang, R.B., Prescott, S.L., Beeler, B., Joshi, N.R., Strohlic, D.E., and Liberles, S.D. (2019). Arterial Baroreceptors Sense Blood Pressure through Decorated Aortic Claws. *Cell Rep.* *29*, 2192–2201.
- Murthy, S.E., Dubin, A.E., and Patapoutian, A. (2017). Piezos thrive under pressure: mechanically activated ion channels in health and disease. *Nat. Rev. Mol. Cell Biol.* *18*, 771–783.
- Murthy, S.E., Dubin, A.E., Whitwam, T., Jojoa-Cruz, S., Cahalan, S.M., Mousavi, S.A.R., Ward, A.B., and Patapoutian, A. (2018a). OSCA/TMEM63 are an Evolutionarily Conserved Family of Mechanically Activated Ion Channels. *eLife* *7*, e41844.
- Murthy, S.E., Loud, M.C., Daou, I., Marshall, K.L., Schwaller, F., Kühnemund, J., Francisco, A.G., Keenan, W.T., Dubin, A.E., Lewin, G.R., and Patapoutian, A. (2018b). The mechanosensitive ion channel Piezo2 mediates sensitivity to mechanical pain in mice. *Sci. Transl. Med.* *10*, eaat9897.
- Nguyen, M.Q., Le Pichon, C.E., and Ryba, N. (2019). Stereotyped transcriptional transformation of somatosensory neurons in response to injury. *eLife* *8*, e49679.
- Olausson, H., Wessberg, J., Morrison, I., McGlone, F., and Vallbo, A. (2010). The neurophysiology of unmyelinated tactile afferents. *Neurosci. Biobehav. Rev.* *34*, 185–191.
- Padilla, F., Couble, M.-L., Coste, B., Maingret, F., Clerc, N., Crest, M., Ritter, A.M., Magloire, H., and Delmas, P. (2007). Expression and localization of the Nav1.9 sodium channel in enteric neurons and in trigeminal sensory endings: implication for intestinal reflex function and orofacial pain. *Mol. Cell. Neurosci.* *35*, 138–152.
- Pan, B., Géléoc, G.S., Asai, Y., Horwitz, G.C., Kurima, K., Ishikawa, K., Kawashima, Y., Griffith, A.J., and Holt, J.R. (2013). TMC1 and TMC2 are components of the mechanotransduction channel in hair cells of the mammalian inner ear. *Neuron* *79*, 504–515.
- Pan, B., Akyuz, N., Liu, X.P., Asai, Y., Nist-Lund, C., Kurima, K., Derfler, B.H., György, B., Limapichat, W., Walujkar, S., et al. (2018). TMC1 Forms the Pore of Mechanosensory Transduction Channels in Vertebrate Inner Ear Hair Cells. *Neuron* *99*, 736–753.
- Patkunarajah, A., Stear, J.H., Moroni, M., Schroeter, L., Blaszkiewicz, J., Tearle, J.L., Cox, C.D., Fürst, C., Sánchez-Carranza, O., Ocaña Fernández, M.D.A., et al. (2020). TMEM87a/Elkin1, a component of a novel mechanoelectrical transduction pathway, modulates melanoma adhesion and migration. *eLife* *9*, e53308.
- Prato, V., Taberner, F.J., Hockley, J.R.F., Callejo, G., Arcourt, A., Tazir, B., Hammer, L., Schad, P., Heppenstall, P.A., Smith, E.S., and Lechner, S.G. (2017). Functional and Molecular Characterization of Mechanosensitive “Silent” Nociceptors. *Cell Rep.* *21*, 3102–3115.
- Price, T.J., and Flores, C.M. (2007). Critical evaluation of the colocalization between calcitonin gene-related peptide, substance P, transient receptor potential vanilloid subfamily type 1 immunoreactivities, and isolectin B4 binding in primary afferent neurons of the rat and mouse. *J. Pain* *8*, 263–272.
- Proske, U., and Gandevia, S.C. (2012). The proprioceptive senses: their roles in signaling body shape, body position and movement, and muscle force. *Physiol. Rev.* *92*, 1651–1697.
- Ranade, S.S., Qiu, Z., Woo, S.H., Hur, S.S., Murthy, S.E., Cahalan, S.M., Xu, J., Mathur, J., Bandell, M., Coste, B., et al. (2014a). Piezo1, a mechanically activated ion channel, is required for vascular development in mice. *Proc. Natl. Acad. Sci. USA* *111*, 10347–10352.

- Ranade, S.S., Woo, S.H., Dubin, A.E., Moshourab, R.A., Wetzel, C., Petrus, M., Mathur, J., Bégay, V., Coste, B., Mainquist, J., et al. (2014b). Piezo2 is the major transducer of mechanical forces for touch sensation in mice. *Nature* **516**, 121–125.
- Ranade, S.S., Syeda, R., and Patapoutian, A. (2015). Mechanically Activated Ion Channels. *Neuron* **87**, 1162–1179.
- Renthal, W., Tochitsky, I., Yang, L., Cheng, Y.C., Li, E., Kawaguchi, R., Geschwind, D.H., and Woolf, C.J. (2020). Transcriptional Reprogramming of Distinct Peripheral Sensory Neuron Subtypes after Axonal Injury. *Neuron* **108**, 128–144.
- Robinson, M.D., McCarthy, D.J., and Smyth, G.K. (2010). edgeR: a Bioconductor package for differential expression analysis of digital gene expression data. *Bioinformatics* **26**, 139–140.
- Roudaut, Y., Lonigro, A., Coste, B., Hao, J., Delmas, P., and Crest, M. (2012). Touch sense: functional organization and molecular determinants of mechanosensitive receptors. *Channels (Austin)* **6**, 234–245.
- Rugiero, F., Drew, L.J., and Wood, J.N. (2010). Kinetic properties of mechanically activated currents in spinal sensory neurons. *J. Physiol.* **588**, 301–314.
- Seal, R.P., Wang, X., Guan, Y., Raja, S.N., Woodbury, C.J., Basbaum, A.I., and Edwards, R.H. (2009). Injury-induced mechanical hypersensitivity requires C-low threshold mechanoreceptors. *Nature* **462**, 651–655.
- Sharma, N., Flaherty, K., Lezgiyeva, K., Wagner, G.E., Klein, A.M., and Ginty, D.D. (2020). The emergence of transcriptional identity in somatosensory neurons. *Nature* **577**, 392–398.
- Syeda, R., Florendo, M.N., Cox, C.D., Kefauver, J.M., Santos, J.S., Martinac, B., and Patapoutian, A. (2016). Piezo1 Channels Are Inherently Mechanosensitive. *Cell Rep.* **17**, 1739–1746.
- Szczot, M., Pogorzala, L.A., Solinski, H.J., Young, L., Yee, P., Le Pichon, C.E., Chesler, A.T., and Hoon, M.A. (2017). Cell-Type-Specific Splicing of Piezo2 Regulates Mechanotransduction. *Cell Rep.* **21**, 2760–2771.
- Szczot, M., Liljencrantz, J., Ghitani, N., Barik, A., Lam, R., Thompson, J.H., Bharucha-Goebel, D., Saade, D., Necaise, A., Donkervoort, S., et al. (2018). PIEZO2 mediates injury-induced tactile pain in mice and humans. *Sci. Transl. Med.* **10**, eaat9892.
- Teng, J., Loukin, S., Anishkin, A., and Kung, C. (2015). The force-from-lipid (FFL) principle of mechanosensitivity, at large and in elements. *Pflugers Arch.* **467**, 27–37.
- Trapnell, C., Pachter, L., and Salzberg, S.L. (2009). TopHat: discovering splice junctions with RNA-Seq. *Bioinformatics* **25**, 1105–1111.
- Usoskin, D., Furlan, A., Islam, S., Abdo, H., Lönnnerberg, P., Lou, D., Hjerling-Leffler, J., Haeggström, J., Kharchenko, O., Kharchenko, P.V., et al. (2015). Unbiased classification of sensory neuron types by large-scale single-cell RNA sequencing. *Nat. Neurosci.* **18**, 145–153.
- Vandewauw, I., De Clercq, K., Mulier, M., Held, K., Pinto, S., Van Ranst, N., Segal, A., Voet, T., Vennekens, R., Zimmermann, K., et al. (2018). A TRP channel trio mediates acute noxious heat sensing. *Nature* **555**, 662–666.
- von Buchholtz, L.J., Ghitani, N., Lam, R.M., Licholai, J.A., Chesler, A.T., and Ryba, N.J.P. (2021). Decoding Cellular Mechanisms for Mechanosensory Discrimination. *Neuron* **109**, 285–298.e5.
- Wang, H., and Zylka, M.J. (2009). Mrgprd-expressing polymodal nociceptive neurons innervate most known classes of substantia gelatinosa neurons. *J. Neurosci.* **29**, 13202–13209.
- Woo, S.H., Lukacs, V., de Nooij, J.C., Zaytseva, D., Criddle, C.R., Francisco, A., Jessell, T.M., Wilkinson, K.A., and Patapoutian, A. (2015). Piezo2 is the principal mechanotransduction channel for proprioception. *Nat. Neurosci.* **18**, 1756–1762.
- Wu, J., Lewis, A.H., and Grandl, J. (2017). Touch, Tension, and Transduction – The Function and Regulation of Piezo Ion Channels. *Trends Biochem. Sci.* **42**, 57–71.
- Xu, J., Mathur, J., Vessières, E., Hammack, S., Nonomura, K., Favre, J., Grimaud, L., Petrus, M., Francisco, A., Li, J., et al. (2018). GPR68 Senses Flow and Is Essential for Vascular Physiology. *Cell* **173**, 762–775.
- Zeisel, A., Hochgerner, H., Lönnnerberg, P., Johnsson, A., Memic, F., van der Zwan, J., Häring, M., Braun, E., Borm, L.E., La Manno, G., et al. (2018). Molecular Architecture of the Mouse Nervous System. *Cell* **174**, 999–1014.
- Zeng, W.Z., Marshall, K.L., Min, S., Daou, I., Chappleau, M.W., Abboud, F.M., Liberles, S.D., and Patapoutian, A. (2018). PIEZO2 mediates neuronal sensing of blood pressure and the baroreceptor reflex. *Science* **362**, 464–467.
- Zheng, Y., Liu, P., Bai, L., Trimmer, J.S., Bean, B.P., and Ginty, D.D. (2019). Deep Sequencing of Somatosensory Neurons Reveals Molecular Determinants of Intrinsic Physiological Properties. *Neuron* **103**, 598–616.

STAR★METHODS

KEY RESOURCES TABLE

Reagent or resource	Source	Identifier
Antibodies		
Anti-Peripherin Antibody	Sigma-Aldrich	CAT# AB1530; RRID:AB_90725
Anti-NFH (NeuroFilament Heavy chain) antibody	AVES Labs	CAT# NFH; RRID:AB_2313552
Alexa Fluor® 647 AffiniPure Donkey Anti-Rabbit IgG (H+L)	Jackson ImmunoResearch	CAT# 711-605-152; RRID:AB_2492288
Rhodamine (TRITC) AffiniPure Donkey Anti-Chicken IgY (IgG) (H+L)	Jackson ImmunoResearch	CAT# 703-025-155; RRID:AB_2340348
Bacterial and virus strains		
XL10-Gold Ultracompetent Cells	Agilent Technologies	CAT# 200314
Chemicals, peptides, and recombinant proteins		
Phosphate buffered saline (PBS)	Sigma-Aldrich	CAT# P4417
PIPES	Sigma-Aldrich	CAT# P6757
HEPES	Sigma-Aldrich	CAT# H3375
EGTA	Sigma-Aldrich	CAT# E4378
Magnesium chloride hexahydrate (MgCl ₂)	Sigma-Aldrich	CAT# M2670
Triton X-100	Sigma-Aldrich	CAT# T8787
Gelatin from cold water fish skin	Sigma-Aldrich	CAT# G7765
Diethyl pyrocarbonate (DEPC)	Sigma-Aldrich	CAT# 159220
Dulbecco's Modified Eagle's Medium (DMEM) High glucose, pyruvate	Thermo Fisher Scientific	CAT# 41966-029
Fetal Bovine Serum (FBS)	GIBCO	CAT# 10270-098
Pen Strep (Penicillin Streptomycin)	GIBCO	CAT# 15140-122
Dulbecco's Phosphate Buffered Saline (DPBS)	GIBCO	CAT# 14190-094
Optimum Cutting Temperature medium	CellPath Ltd	CAT# KMA-0100-00A
Isoflurane	IsoVet	CAT# 200265
Sucrose	Sigma-Aldrich	CAT# S0389
16% Formaldehyde (w/v), Methanol-free	Thermo Fisher Scientific	CAT# P128908
ProLong Gold Antifade Mountant	Thermo Fisher Scientific	CAT# P36930
Thermo Scientific SuperFrost Plus Adhesion slides	Thermo Fisher Scientific	CAT# J1800AMNZ
GelRed Nucleic Acid Gel Stain, 10,000X	Biotium	CAT# 41003
ExactGene 100bp ladder	Fisher BioReagents™	CAT# BP2571100
Critical commercial assays		
RNAscope fluorescent multiplex reagent kit	Advanced Cell Diagnostics	CAT# 323133
RNAscope Protease IV Reagent	Advanced Cell Diagnostics	CAT# 322340
Fluorescent Multiplex Detection Reagents	Advanced Cell Diagnostics	CAT# 320851
Wash Buffer Reagents	Advanced Cell Diagnostics	CAT# 310091
NucleoSpin RNA Mini kit	Macherey-Nagel	CAT# 740955
SMART Ultra Low Input RNA kit v4	Clontech Laboratories, Inc.	CAT# 634888
AMPure XP beads	Beckman Coulter Genomics Inc.	CAT# A63881
Nextera XT DNA Library Prep Kit	Illumina, Inc.	CAT# FC-131-1024
DNA-free DNase Treatment	Ambion	CAT# AM1906
iScript™ Reverse Transcription Supermix for RT-qPCR	Bio-Rad	CAT# 1708840
KAPA SYBR® FAST qPCR Kit Master Mix (2X) Universal	Kapa Biosystems Ltd	CAT# KK4600

(Continued on next page)

Continued

Reagent or resource	Source	Identifier
Neon Transfection System 10 μ L Kit	Invitrogen	CAT# MPK1096
Deposited data		
Raw single cell RNaseq-data	This paper	GEO: GSE168032
Experimental models: Cell lines		
NIH 3T3	ATCC	CAT# CRL-1658 ; RRID: CVCL_0594
HEK P1/KO - PIEZO1-deficient HEK293T cells	Dubin et al., 2017	N/A
Experimental models: Organisms/strains		
C57BL/6J mice	The Jackson Laboratory ; bred	RRID: IMSR_JAX:000664
Oligonucleotides		
<i>Tmem120a</i> probe	Advanced Cell Diagnostics	CAT# 513211
RNAscope 3-plex Negative Control Probe	Advanced Cell Diagnostics	CAT# 320871
ON-TARGETplus Mouse <i>Piezo2</i> siRNA	Horizon Discovery	CAT# L-163012-00-0005
ON-TARGETplus Mouse <i>Tmem120a</i> siRNA	Horizon Discovery	CAT# L-040281-01-0005
FlexiTube GeneSolution <i>Tmem150c</i> siRNA	QIAGEN	CAT# GS231503
ON-TARGETplus Mouse Non-targeting Control Pool	Horizon Discovery	CAT# D-001810-10-05
<i>Piezo1</i> Forward Primer Sequence: ATGCCATCATCTGGTTCCC	Genewiz	N/A
<i>Piezo1</i> Reverse Primer Sequence: CTAGCTTGAGGGTGACGGTG	Genewiz	N/A
<i>Piezo2</i> Forward Primer Sequence: CCAAAGTCAATGGTCGCGTG	Genewiz	N/A
<i>Piezo2</i> Reverse Primer Sequence: CAAGGCTGGCCGTCATATTC	Genewiz	N/A
<i>Tmem120a</i> Forward Primer Sequence: GGCAACTCTTCAATGCGCTGAC	Genewiz	N/A
<i>Tmem120a</i> Reverse Primer Sequence: ACTTCTGATGCACCACTCGCAG	Genewiz	N/A
<i>Tmem150c</i> Forward Primer Sequence: GTCAATATCAAGAACGAGGGG	Genewiz	N/A
<i>Tmem150c</i> Reverse Primer Sequence: AATACAGGACTACGCAGAGG	Genewiz	N/A
<i>Gapdh</i> Forward Primer Sequence: GCAAATCAACGGCACA	Genewiz	N/A
<i>Gapdh</i> Reverse Primer Sequence: CACCAGTAGACTCCACGAC	Genewiz	N/A
<i>Actb</i> Forward Primer Sequence: GCCAACC GTGAAAAGATGAC	Genewiz	N/A
<i>Actb</i> Reverse Primer Sequence: GGCGTGAGGGAGAGCATAG	Genewiz	N/A
Recombinant DNA		
pIRES2-AcGFP1	Clontech Laboratories, Inc.	CAT# 632435
Software and algorithms		
Clampfit 10.7	Molecular Devices	RRID: SCR_011323
ImageJ 1.50b	NIH	RRID: SCR_003070
GraphPad Prism 8.0.2	GraphPad Software	RRID: SCR_015807
R/Bioconductor 3.12	www.bioconductor.org	RRID: SCR_006442
edgeR 3.30.3	Robinson et al., 2010	RRID: SCR_012802
CutAdapt 1.9.1	Martin, 2011	RRID: SCR_011841
TopHat-2 2.1.0	Trapnell et al., 2009	RRID: SCR_013035

(Continued on next page)

Continued

Reagent or resource	Source	Identifier
GenomicAlignment 1.24.0	Lawrence et al., 2013	N/A
Batchelor 1.4	Haghverdi et al., 2018	RRID: SCR_017351
Other		
Applied Biosystems 7500 Fast Real-Time PCR System	Applied Biosystems	N/A

RESOURCE AVAILABILITY

Lead contact

Further information and requests for reagents and resources should be directed to and will be fulfilled by the lead contact, Bertrand Coste (bertrand.coste@univ-amu.fr).

Materials availability

This study did not generate new unique reagents.

Data and code availability

- The single-cell RNA-seq datasets generated and analyzed have been deposited in NCBI's Gene Expression Omnibus and are publicly available through the following GEO Series accession numbers: GEO: GSE168032.
- This paper does not report original code.
- Any additional information required to reanalyze the data reported in this work paper is available from the lead contact upon request.

EXPERIMENTAL MODEL AND SUBJECT DETAILS

Animals

All animals were used in accordance with the European Community guidelines in the care and use of animals (2010/63/UE). Male mice (C57BL/6J background) were 10-12 weeks old. Animals were housed in a 12h light /12h dark cycle and fed *ad libitum*. This project was approved by the Institutional Review Board of the regional ethic committee.

Dorsal root ganglion neuron culture

Mice were anesthetized with isoflurane and killed by decapitation. DRG were isolated and incubated in enzyme solution containing 2 mg.mL⁻¹ of collagenase 1A (Sigma-Aldrich) and 5 mg.mL⁻¹ of dispase II (ThermoFisher) for 45 min at 37 °C. The tissue was washed several times and triturated in Hanks' balanced salt solution (HBSS, GIBCO). The resulting suspension was centrifuged (300 × g for 5 min) in 1 mL HBSS and 1 mL Bovine Serum Albumin (BSA, 15%, Sigma-Aldrich). The pellet was rinsed with Dulbecco's Phosphate Buffered Saline (DPBS, GIBCO) and centrifuged (300 × g for 2 min). Cells were then plated onto poly-D-lysine-coated 12-mm round glass coverslips (Corning) in 24-well plates and were grown in Dulbecco's modified Eagle's medium (DMEM, High glucose, pyruvate, ThermoFisher) supplemented with 10% heat-inactivated Fetal Bovine Serum (FBS, GIBCO), 100 U.mL⁻¹ (1%) penicillin-streptomycin (GIBCO), 100 ng.mL⁻¹ nerve growth factor (NGF, Merk Millipore), and 50 ng.mL⁻¹ glial-derived neurotrophic factor (GDNF, ThermoFisher). Cells were recorded at 3-5 days *in vitro* (DIV).

Cell lines

NIH/3T3 cells and PIEZO1-deficient HEK293T cells ([Dubin et al., 2017](#)) were grown in DMEM supplemented with 10% heat-inactivated FBS (GIBCO) and 100 U.mL⁻¹ (1%) penicillin-streptomycin (GIBCO) and cultured in 37°C with 5% CO₂. Cell passage was done when cells reached 80% confluency. For recordings, cells were plated onto poly-D-lysine-coated 12-mm round glass coverslips (Corning) in 24-well plates.

METHOD DETAILS

Electrophysiology

Patch-clamp experiments were performed under whole-cell configuration using an Axopatch 200B amplifier (Axon Instruments). Patch pipettes had resistances of 2-3 MΩ when filled with an internal solution consisting of (in mM) 140 CsCl, 10 HEPES, 5 EGTA, 1 CaCl₂, 1 MgCl₂, 4 MgATP and 0.4 Na₂GTP (pH adjusted to 7.3 with CsOH). Internal solution was supplemented with 0.4 U/μL

of RNaseOUT (Invitrogen) for cell harvesting experiments. The extracellular solution consisted of (in mM) 133 NaCl, 3 KCl, 1 MgCl₂, 10 HEPES, 2.5 CaCl₂, 10 glucose (pH adjusted to 7.3 with NaOH). All experiments were done at room temperature. Currents were sampled at 20 kHz and filtered at 2 kHz.

Mechanical stimulation

Mechanical stimulation was achieved using a firepolished glass pipette (tip diameter 3–4 μm) positioned at an angle of 80° and in contact with the cell being recorded. Downward movement of the probe toward the cell was driven by a Clampex controlled piezo-electric crystal microstage (E625 LVPZT Controller/Amplifier, Physik Instrumente). The probe had a velocity of 0.7 μm.ms⁻¹ during the ramp segment of the command for forward motion, and the stimulus was applied for 150 ms. Inward MS currents were recorded at a holding potential of –80 mV.

MS currents were characterized by applying series of 0.5 μm incremental steps every 10 s. This was done up to patch rupture, except for neurons dedicated to scRNaseq experiments. For this set of experiments, mechanical stimulation of neurons was stopped after MS currents with a peak amplitude of more than 100 pA were elicited in at least two consecutive incremental steps, preserving the integrity of the cellular content before the harvesting. The 3 non-responsive neurons included in our scRNaseq sample have been mechanically stimulated up to 10 μm probe displacement without disrupting the patch.

Pressure-clamp experiments

Pressure-clamp experiments were performed under cell-attached configuration. Patch pipettes had resistances of 2–3 MΩ when filled with a solution consisting of (in mM) 130 NaCl, 5 KCl, 10 HEPES, 1 CaCl₂, 1 MgCl₂, 10 TEA-Cl (pH 7.3 with NaOH). External solution used to zero the membrane potential consisted of (in mM) 145 KCl, 10 HEPES, 1 MgCl₂, 10 glucose (pH 7.3 with KOH). Currents were sampled at 20 KHz and filtered at 2 KHz. Membrane patches were stimulated with negative pressure pulses through the recording electrode using a Clampex controlled pressure clamp HSPC-1 device (ALA-scientific). Stretch-activated channels were recorded at a holding potential of –80 mV.

Single-cell library preparation

After electrophysiological recording, the cytoplasmic content of the neuron was harvested into the patch pipette, transferred into lysis solution (RNaseOUT 8 U.μL⁻¹, 2% Triton X-100) and flash frozen. Reverse transcription was performed using a SMART-seq v4 Low Input Kit (Clontech) directly on the cell lysate according to the manufacturer's protocol. After cDNAs amplification, 50 μL of the sample were subjected to cDNA purification on AMPure XP beads. 0.5 ng of each purified cDNAs were used to construct the sequencing library using Nextera XT kit (Illumina) with fragments over 300-bp length from each neuron.

Processing, quality control and filtering of single-cell RNA-seq data

cDNA libraries were sequenced either in a NextSeq 500 (Illumina) using paired-end reads (76 pb) with an average depth of 29 million reads per cell. The raw reads (FastQ files) were cleaned by removing adaptor sequences, short sequences (length < 25 bp), low-quality bases (quality score < 30) and ambiguous sequences (i.e., reads with more than 30% unknown bases 'N') using CutAdapt 1.9.1 software (Martin, 2011). TopHat-2 v2.1.0 was used to map the cleaned RNA-seq reads to the mouse genome (mm10 / GRCm38.90) with two mismatches, two gaps and one multihit allowed. TopHat-2 splicing algorithm was used to map reads covering splice junctions, thereby improving the utilization of reads. After genome mapping, gene counts matrix was determined using GenomicAlignment (version 1.24.0) (Lawrence et al., 2013) using GTF annotation. A set of mitochondrial genes (mt-Atp6, mt-Atp8, mt-Co1, mt-Co2, mt-Co3, mt-Cytb, mt-Nd1, mt-Nd2, mt-Nd3, mt-Nd4, mt-Nd4l, mt-Nd5, mt-Nd6) were used to check viability of each sample: the sample is considered as non-apoptotic if the expression of these genes is less than 10% of total count in the same cell. Read counts were analyzed in the R/Bioconductor environment (version 3.12; www.bioconductor.org) with the R package edgeR. The gene expression value was normalized between samples by TMM with a gene detection threshold of 20 counts in at least two cells. For the generation of heatmaps shown in Figure 2B, z-transformed TMM count data was used. Relative expression levels were obtained by sample normalization using TPM (transcripts per kilobase million).

Dorsal root ganglion neuron clustering

The mapping of the scRNaseq neurons in DRG neuron transcriptional clusters was done by a cross-dataset normalization approach. We used fastMNN, the new implementation of Mutual Nearest Neighbors (MNN) correction (Haghverdi et al., 2018) implemented in the R package batchelor to combine our dataset with Zeisel and collaborators scRNaseq sensory neuron dataset (Zeisel et al., 2018). Briefly, a principal component analysis (PCA) was performed on the 211 most highly variable genes in DRG neurons (most highly enriched genes for each cluster) (Zeisel et al., 2018) to correct for batch effect. Identification of MNN was done in this reduced dimension space using the following parameters: dimension = 60 and k = 10. To assign each individual neuron to a specific cluster, we built a k nearest-neighbors (kNN) graph with k = 28 using Euclidean distance. Individual neurons were first assigned to one of the main cluster: NF, NP or PEP. Next, we repeated the procedure (PCA implemented in MNN correction, kNN clustering) for each main cluster. We were able to assign each cell to a specific sub-cluster: PSNF1, PSNF2, PSNF3, PSNP1, PSNP2, PSNP3, PSNP4, PSNP5, PSNP6, PSPEP1, PSPEP2, PSPEP3, PSPEP4, PSPEP5, PSPEP6, PSPEP7 or PSPEP8. Corrected expression values obtained during this procedure were only used for cluster assignment and

visualization with t-distributed stochastic neighbor embedding (tSNE) projection (perplexity = 30, max iteration = 1000). Downstream analysis was performed using custom R scripts.

Electroporation

DRG cultures were electroporated using the Neon® Transfection System (Invitrogen) according to the manufacturer's protocol. After the centrifugation prior to cell plating, the cell pellet was resuspended in Neon® Transfection System resuspension Buffer R (Invitrogen) and gently mixed with 30 ng.μL⁻¹ of pIRES2-AcGFP1 plasmid (*Aequorea coerulescens* GFP, Clontech; referred in results as GFP-plasmid) and 250 nM siRNA pool. Ten microliters of the cell suspension were then electroporated with the following program: 1200 V, 2 pulses, 20 ms. Electroporated cells were then plated onto poly-D-Lysine-coated 12-mm round glass coverslips in 24-well plates in antibiotics-free media. Three hours later, the medium was replaced by DMEM supplemented with 10% heat-inactivated FBS, 1% penicillin–streptomycin, 100 ng.mL⁻¹ NGF and 50 ng.mL⁻¹ GDNF. Pools of 4 siRNAs targeting *Piezo2* or *Tmem120a*, or non-targeting siRNA for control experiments were purchased at Horizon Discovery (#L-163012-00-0005, #L-040281-01-0005 and #D-001810-10-05 for *Piezo2*, *Tmem120a* and control siRNA, respectively) and the pool of 4 siRNAs targeting *Tmem150c* was purchased at QIAGEN (#GS231503). Media were changed 48 hours later. Transfected DRG neurons were visualized by the expression of GFP. For experiments performed on IB4-positive neurons, neurons were incubated with 1 μg.mL⁻¹ isolectin GS-IB4 from Griffonia simplicifolia, AlexaFluor 568 conjugate (Invitrogen) at 37°C for 10 minutes before recording.

NIH/3T3 cells were electroporated using the Neon® Transfection System (Invitrogen) according to the manufacturer's protocol. Briefly, prior to cell plating, the cell pellet was resuspended in Neon® Transfection System Buffer R at a cell density of 1 × 10⁷ cells.mL⁻¹. 250 nM siRNA was added to 10 μL of cell suspension and electroporation was done with the following program: 1400 V, 1 pulse, 30 ms. Electroporated cells were then transferred directly into 24-well tissue culture plates (1 × 10⁵ cells per well) for RNA extraction, or onto poly-D-lysine-coated 12-mm round glass coverslips for patch-clamp recording experiments 72 hours later.

Molecular cloning of *Tmem120a*

Primers were designed from cDNA sequence of *Tmem120a* from the NCBI database (NM_172541). A 1.096 kb fragment was amplified from cDNA libraries generated from adult C57BL/6J DRG total RNA using primers fwd (5' GATTATGCATGCCGTGGACAAAGA CATGCAGT 3') and rev (5' GATTATGGATCCTCAGTCCTTCTTGTCCCGT 3') and cloned into pIRES2-AcGFP1 vector (Clontech, #632435) with NheI and BamHI restriction sites. The protein sequence of *Tmem120a* that we cloned is identical to NCBI Reference Sequence NP_766129.

Transfection of HEK-P1KO cells

PIEZO1-deficient HEK293T cells (Dubin et al., 2017) were transfected using lipofectamine 2000 (Invitrogen) according to the manufacturer's instruction. Each well was transfected with 600 ng.mL⁻¹ of specified constructs. GFP positive cells were recorded 48 hours later.

qRT-PCR experiments

Electroporated NIH/3T3 cells were harvested after 48 hours of incubation at 37°C in antibiotics-free growth medium. Total RNA was extracted using NucleoSpin RNA Mini kit (Macherey-Nagel) according to the manufacturer's instructions. DNA-free DNase Treatment (Ambion) was additionally used to remove genomic DNA contamination and iScript™ Reverse Transcription Supermix for qRT-PCR (Bio-Rad) was employed for cDNA synthesis. Samples generated with the iScript No-RT Control Supermix included in the kit were also synthesized for each sample as an additional verification step for the absence of genomic DNA contamination.

DRG neurons were electroporated and cultured as described above. Forty-eight hours later, GFP-expressing DRG neurons were harvested individually and transferred into lysis solution (RNaseOUT 8 U.μL⁻¹, 2% Triton X-100). For each condition, 4 pools of 5 neurons were collected and flash frozen. Reverse transcription was performed using a SMART-seq v4 Low Input Kit (Clontech) directly on the cell lysates according to the manufacturer's protocol.

Quantitative PCR (qPCR) was performed on an Applied Biosystems 7500 Fast Real-Time PCR System (Applied Biosystems) using KAPA SYBR® FAST qPCR Kit Master Mix (2X) Universal (Kapa Biosystems). A 12 μL reaction mix was made using 4 μL of diluted cDNA template (1 ng/μL for NIH/3T3 cells and 10 ng/μL for DRG neurons), specific primers (200 nM each), ROX Reference Dye Low (0.24 μL) and SYBR Green I Master Mix (6 μL) as recommended by the manufacturer. Cycling conditions were as follows: 95°C for 3 s, then 60°C for 30 s, 40 cycles. Reactions were performed in duplicate and melting-curve analysis was performed to assess the specificity of each amplification. *Actb* and *Gapdh* were selected as reference genes.

qRT-PCR amplicons produced in the presence or absence of RT enzyme were size-separated by electrophoresis on a 3.5% agarose gel stained with GelRed (Biotum), in comparison with ExactGene 100 bp ladder (Fisher BioReagents™) and photographed under UV light. The expected amplicon sizes are 144 bp for *Tmem120a*, 100 bp for *Piezo1*, 99 bp for *Piezo2* and 85 bp for *Tmem150c*.

In Situ Hybridization experiments

Mice were anesthetized with isoflurane and killed by decapitation. Thoraco-lumbar vertebral spines were freshly collected, cut transversely, and transferred to a 4% sucrose solution (in 1X PBS) during 1h30 at 4°C, then to a 20% sucrose solution (in 1X PBS) overnight

at 4°C. Then, DRG were isolated and embedded in Optimum Cutting Temperature medium (OCT; CellPath Ltd; #KMA-0100-00A) and cut into 14 μm sections with a CM350 S cryostat (Leica). *In situ* hybridization (ISH) was carried out using the RNAscope fluorescent multiplex reagent kit (Advanced Cell Diagnostics, a Bio-Techne brand, United States; #323133), according to the manufacturer's instructions. Briefly, tissue sections were post-fixed with 4% paraformaldehyde during 30 min at 4°C and rinsed with 1X PBS. After ethanol dehydration and a Protease IV pretreatment for 30 minutes at room temperature, sections were incubated with a mouse *Tmem120a* probe (ACD; #513211, accession number #NM_172541.2) for 2h at 40°C. The negative control, designed by ACD Bio, contains probes targeting the *DapB* gene from the *Bacillus subtilis* strain SMY (ACD; #320871, accession number #EF_191515). The signal was amplified with a succession of four pre-amplifiers supplied in the kit and detected with Alexa 488.

Immunofluorescence staining

NF-200 and peripherin immunostainings were done following ISH. After washing for 10 min at room temperature with PHEM buffer (consisting of in mM: 60 Pipes, 25 HEPES, 10 EGTA, 2 MgCl₂) supplemented with 0.1% Triton X-100, non-specific sites were blocked with a reagent containing 3% Gelatin from cold water fish skin (Sigma-Aldrich; #G7765). Samples were incubated with primary antibodies against peripherin (1:200; rabbit polyclonal; Sigma-Aldrich; #AB1530) and NF-200 (1:1000; chicken polyclonal; AVES Labs; #NFH) overnight at 4°C. Primary antibodies were detected by using secondary antibodies conjugated to Alexa Fluor 647 (1:1000; Donkey anti-rabbit polyclonal IgG; Jackson ImmunoResearch, #711-605-152) and Alexa Fluor 568 (1:1000; Goat anti-chicken polyclonal IgY; Invitrogen, #A-11041), respectively, incubated for 1 h at room temperature. Sections were rinsed with PHEM buffer, dried and mounted in Prolong Gold Antifade Mountant (ThermoFisher; #P36930).

Gene Ontology (GO)

Gene Ontology (GO) annotations (Ashburner et al., 2000; Gene Ontology, 2021) were determined using the R package limma (v.3.44.3) and custom R scripts. GO terms were taken from the Bioconductor annotation package org.Mm.eg.db (v.3.11.4) released on 2020-05-02. The following GO terms were selected: detection of mechanical stimulus (GO:0050982), ion channel activity (GO:0005216) and integral component of membrane (GO:0016021).

QUANTIFICATION AND STATISTICAL ANALYSIS

Mechanosensitive current analysis

Clampfit 10.7 (Molecular Devices) software was used to analyze recordings and biophysical parameters. The decay of inactivation from the peak of current was fitted with mono or bi-exponential function of the form $f(t) = \sum_{i=0}^n A_i e^{-t/\tau_i} + C$. C was set to the baseline value of current once the mechanical stimulus is removed. Inactivation time constant τ was used to identify the type of MS current components. To note, τ measurements of ultra-SA currents are approximate due to the relative short lasting (150 ms) of the mechanical stimulus. When fitted with bi-exponential equation, the contribution (in percentage) of each component to the whole current is determined from the ratio of A_i to the amplitude of the peak current (see Figure S2B). Recordings of MS currents displaying no clear deactivation once the mechanical stimulus is removed were discarded. We arbitrarily set a component detection threshold at 10% of the peak current, i.e., so that only detected components contributing to at least 10% of MS currents were included into analyzes, to avoid mis-identification of current components.

Differential expression analysis

Analysis of differential gene expression was made between the cells expressing a given type of MS current (RA, IA, SA or ultra-SA current) versus cells that do not express this specific current (control group). LogP value is the Pvalue of Fold Change determined with exact test for negative binomial distribution implanted in the R package edgeR between two groups of count libraries. We set up a 2-fold enrichment threshold (with Pvalue < 0.05) to consider genes displaying expression enrichment in the group of interest compared to the control group. For graphical representation, fold change is displayed as Log2 values (corresponding to Log2FC) and Pvalue as -log10 values (corresponding to -Log10 Pvalue).

Abundance of transcripts is expressed by the Transcript Per kilobase Million value (TPM). Mean TPM values in a group of neurons expressing a specific current type can be used to rank genes by transcript abundance in this group, which differs from fold change values that do not consider absolute level of expression but reflect expression difference between two groups. In Figure 6, we used both parameters to present gene candidates, i.e., we listed among genes that are significantly enriched (FC > 2, Pvalue < 0.05) in the group of interest those that are the most abundantly expressed in this group (ranked by mean TPM).

qPCR Analysis

For each sample, Ct values obtained for gene of interest (GOI) were normalized in relation to the average Ct values of *Gapdh* and *Actb* genes (RG) ($\Delta Ct = Ct_{GOI} - \text{Mean } Ct_{RG}$). The difference between the ΔCt of the sample of interest and the control sample ($\Delta \Delta Ct = \Delta Ct_{\text{sample of interest}} - \Delta Ct_{\text{control sample}}$) was then calculated, and finally the $2^{-\Delta \Delta Ct}$ value to express the results as relative expression levels of gene of interest in samples of interest versus the control sample (non-targeting siRNA).

Image Acquisition and Analysis

Images were acquired using a LSM 780 laser-scanning confocal microscope (Zeiss) with Ar and He-Ne lasers using a 63X oil-immersion objective. Images were treated and analyzed with ImageJ software (v 1.50b, NIH, United States). The “analyze particle” function was used to quantify *in situ* hybridization signal. Neurons containing at least two dots were considered positive.

STATISTICAL ANALYSIS

Unless mentioned otherwise in Method Details above, data were analyzed using GraphPad Prism 8.2.0 (San Diego, USA). Statistical details can be found in the figure legends and in the main text. Reported n values can be found in the figure legends and in the results. All data are represented as mean \pm s.e.m. (standard error of mean) unless indicated otherwise. All replicates were biological. No statistical methods were used to pre-determine sample sizes. All statistical tests are indicated in the respective figure legend and are two-sided. In all figure legends the exact value and definition of n is indicated. In all panels: not significant, ns $p > 0.05$; * $p < 0.05$; ** $p < 0.01$; *** $p < 0.001$.

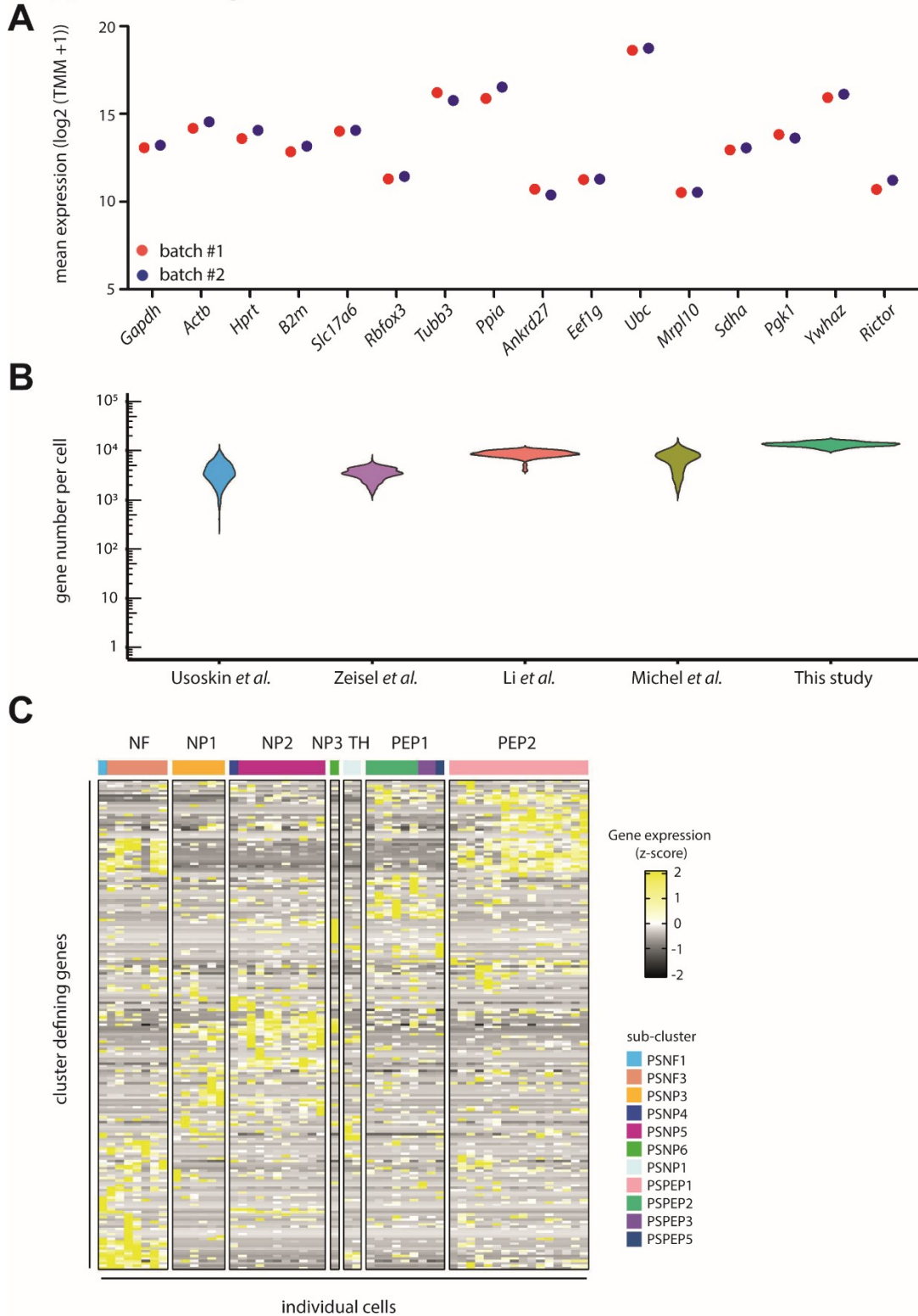
Cell Reports, Volume 37

Supplemental information

**Patch-seq of mouse DRG neurons
reveals candidate genes for
specific mechanosensory functions**

Thibaud Parpaite, Lucie Brosse, Nina Séjourné, Amandine Laur, Yasmine Mechioukhi, Patrick Delmas, and Bertrand Coste

Supplemental figure 1

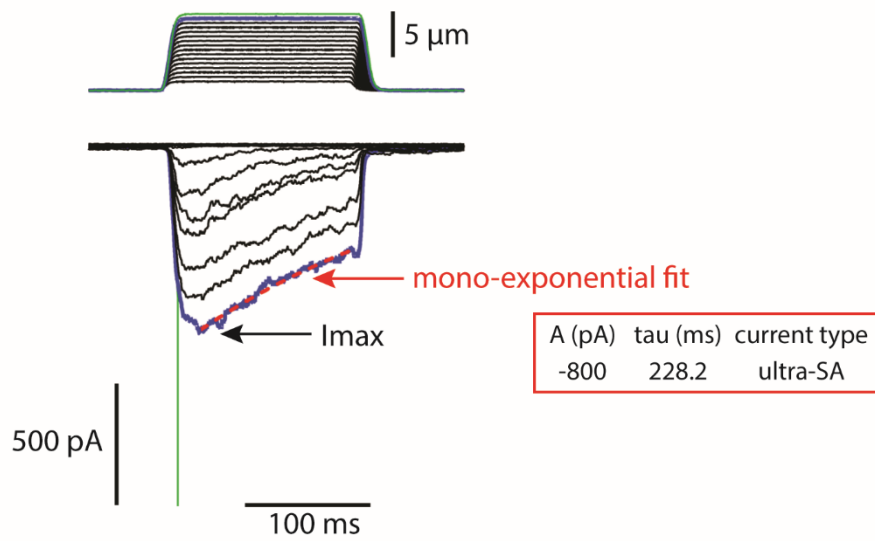


Supplemental Figure 1. RNA Sequencing Data Quality, related to Figure 2.

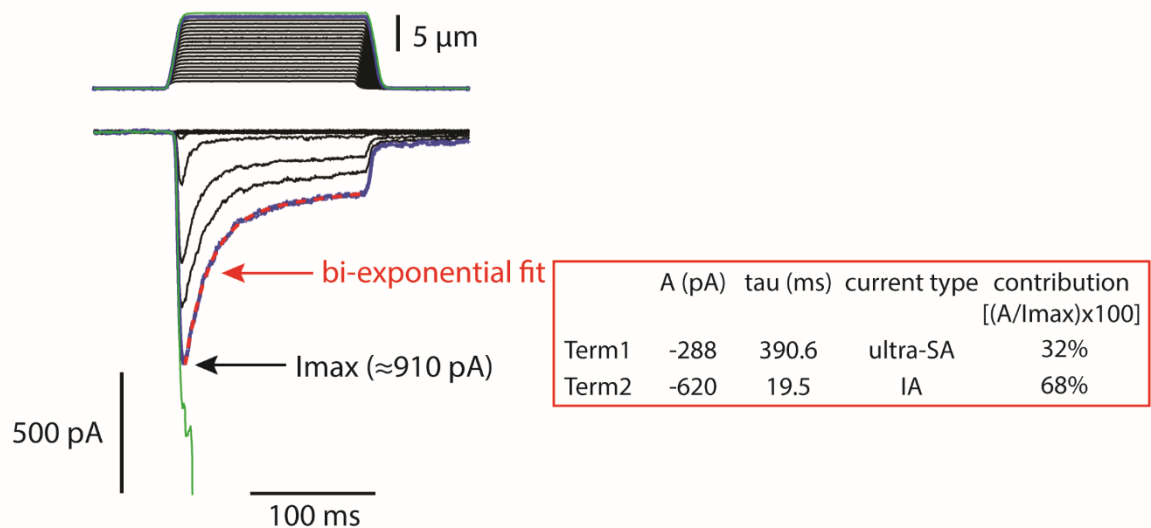
(A) Expression levels of representative reference genes of the two sequencing batches. Data shown are means of \log_2 transformed TMM+1 values. (B) Violin plot of number of expressed genes per DRG neuron in DRG RNA sequencing studies, as indicated. Expressed genes are set with a threshold of $\text{TPM} \geq 1$ except for Usoskin dataset for which the threshold is $\text{CPM} \geq 1$. (C) Heat map of expression of the 211 genes used for DRG neuron clustering (see Fig.2A).

Supplemental figure 2

A



B

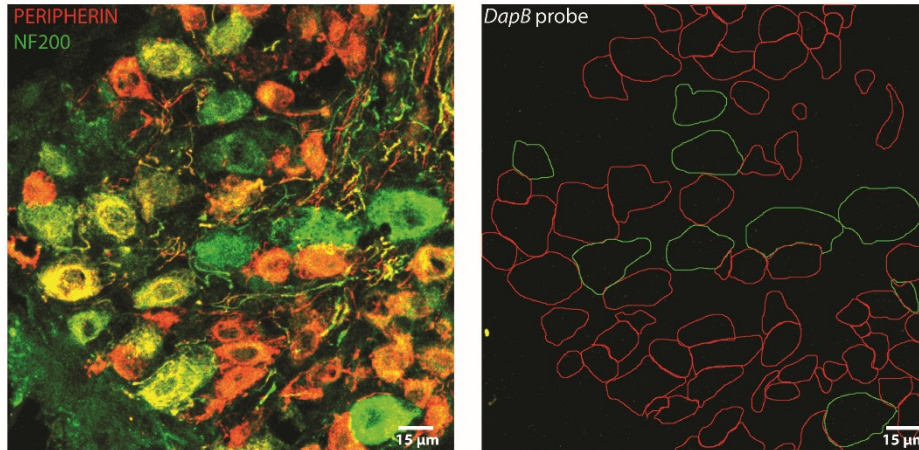


Supplemental Figure 2. Analysis of mono- and bi-phasic MS currents, related to Figure 1 B, C and D.

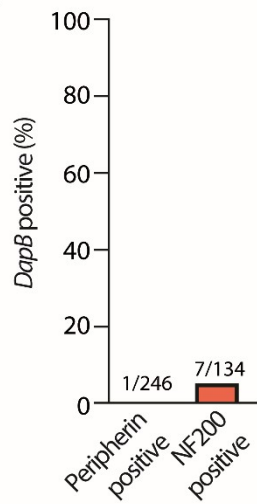
Typical current traces of monophasic (A) and biphasic (B) MS currents. Currents were elicited by increasing mechanical stimulus up to patch rupture (green traces). Inactivation kinetics were fitted with mono- (A) or bi-exponential (B) equation (red dashed lines), giving fitting parameters as depicted. Tau values were used to classify MS current types. For biphasic currents, the contribution of each MS current type is determined from the ratio $(A/I_{max}) \times 100$.

Supplemental figure 3

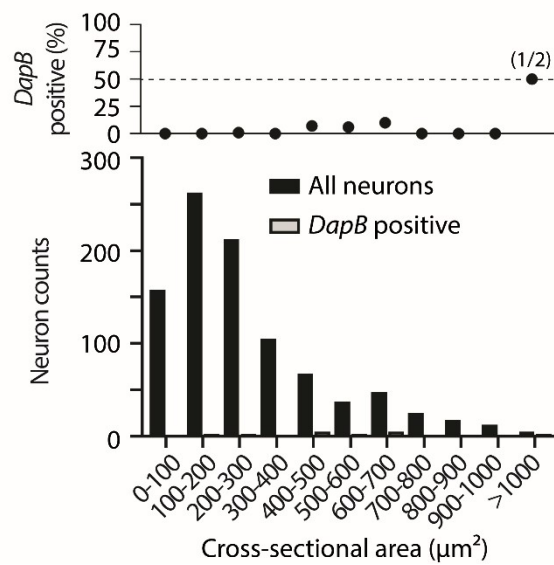
A



B



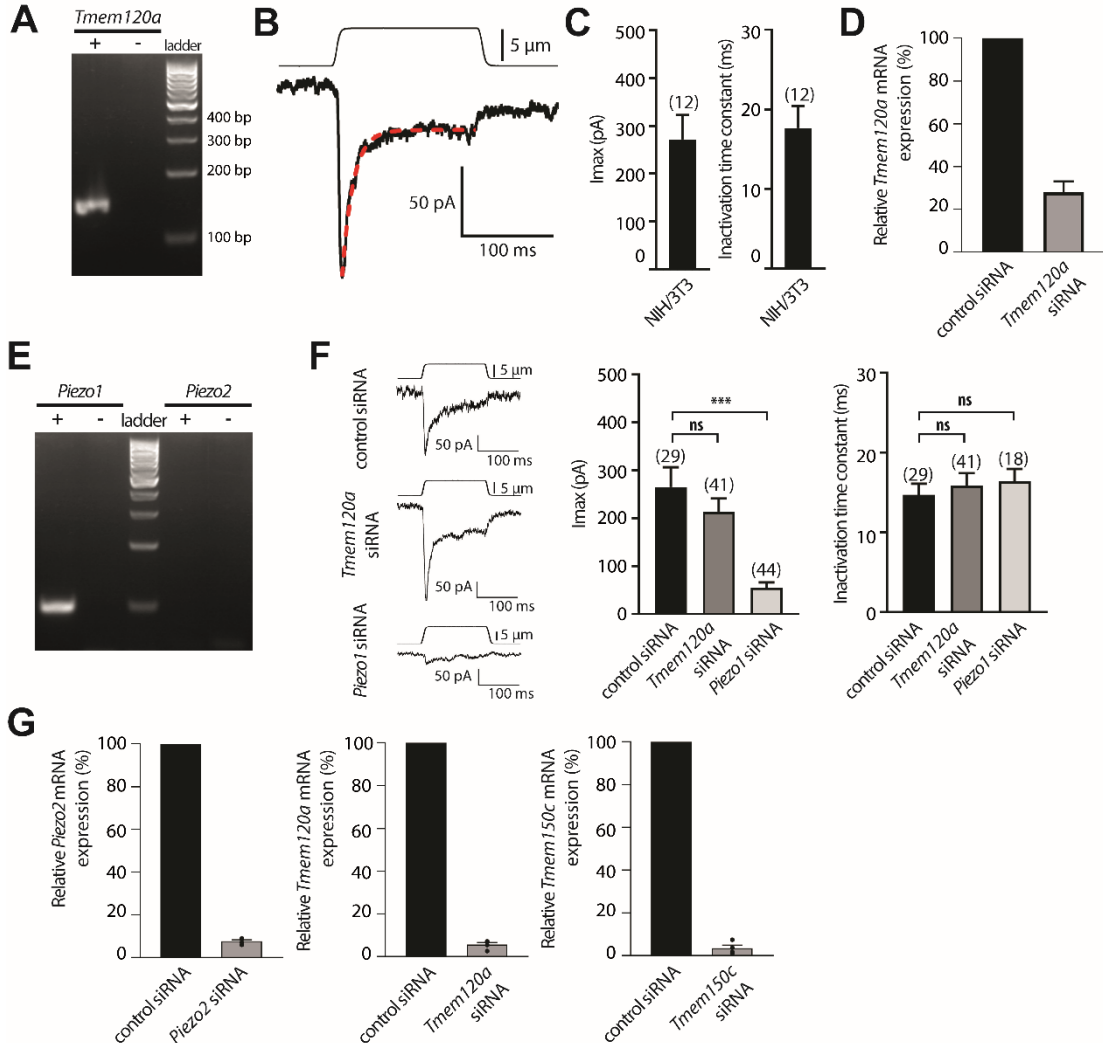
C



Supplemental Figure 3. *In Situ* Hybridization negative control, related to Figure 5A-C.

(A) Representative images of fluorescent *in situ* hybridization for the control gene *DapB* (right panel) in DRG neurons immuno-stained for peripherin and NF200 (left panel). (B) Percentage of *ISH* positive DRG neurons in Peripherin- and NF200- positive populations. (C) Cross-sectional area distribution of *DapB* mRNA positive neurons. Top panel shows the percentage of *DapB* positive neurons.

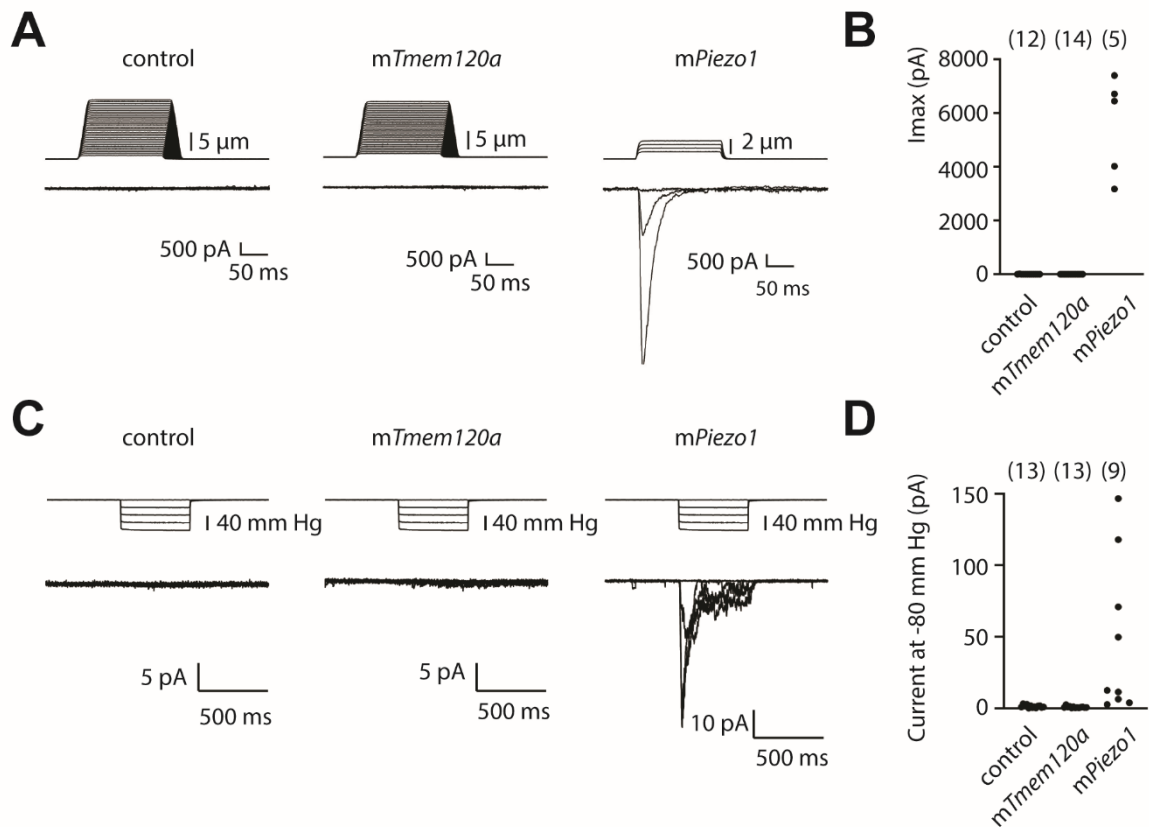
Supplemental figure 4



Supplemental Figure 4. Efficacy of siRNAs in NIH/3T3 cells and DRG neurons, related to Figure 5D-G

(A) PCR products in NIH/3T3 cells using *Tmem120a* specific primers from reverse transcription done in the presence (+) or absence (-) of RT enzyme. (B) Representative recording of a MS current elicited at a holding potential of -80 mV in NIH/3T3 cells. Red dashed line represents fit of inactivation with a mono-exponential equation ($\tau = 11.7$ ms). (C) Average maximal amplitude (left panel) and time-constant of inactivation (right panel) of NIH/3T3 MS current elicited at holding potential of -80 mV. N numbers are indicated in brackets. Error bars represent s.e.m. (D) Expression of *Tmem120a* mRNA in NIH/3T3 cells determined by RT-qPCR 48h after electroporation with control or *Tmem120a* siRNA ($n = 2$, *Gapdh* and β -actin as reference genes). Electroporated and unelectroporated cells are not sorted leading to underestimation of down-regulation. (E) PCR products in NIH/3T3 cells using *Piezo1* and *Piezo2* specific primers from reverse transcription performed in the presence (+) or absence (-) of RT enzyme. (F) Typical recording traces (left panels), average maximal amplitude (middle panel) and time-constant of inactivation (right panel) of MS currents elicited at holding potential of -80 mV in NIH/3T3 cells transfected with control, *Tmem120a* or *Piezo1* siRNA. In panel B and F, upper traces represent the mechanical probe displacement and lower traces the recorded currents. N numbers are indicated in brackets. Error bars represent s.e.m.; ***, $p < 0.001$; ns, not significant; Kruskal-Wallis multiple comparison test. (G) Relative expression of *Piezo2*, *Tmem120a* and *Tmem150c* mRNAs determined by RT-qPCR in DRG neurons 48h after electroporation with control or targeting siRNA (*Gapdh* and β -actin as reference genes). Electroporated cells identified by GFP fluorescence were manually sorted and sampled in 4 pools of 5 cells per condition.

Supplemental figure 5



Supplemental Figure 5. Overexpression of mouse *Tmem120a* does not induce MS current in HEK-P1KO cells, related to Figure 5D-G

(A) Representative examples of recordings in cells voltage clamped at -80 mV and stimulated with a mechanical probe under whole-cell configuration. Cells were transiently transfected with control vector, *Tmem120a* or *Piezo1*, as specified. (B) Maximal MS current amplitude in each stimulated cell. N numbers are in brackets. (C) Representative examples of recordings in cell-attached patches stimulated with pulses of negative pressure applied in the recording pipette. Cells were transiently transfected with control vector, *Tmem120a* or *Piezo1*, as specified. (D) Maximal MS current amplitude elicited with -80 mm Hg stimulation step in each stimulated cell. N numbers are in brackets.

Cell number	Neuron type	Genetic cluster (Nomenclature from Zeisel <i>et al.</i> , 2018)	Mixed currents	Current type 1 (major)	Current type 2 (minor)	Proportions [type1 (%) / type2 (%)]
1	NF	PSNF1	NO	RA		
2	NF	PSNF3	NO	RA		
3	NF	PSNF3	NO	RA		
4	NF	PSNF3	NO	RA		
5	NF	PSNF3	NO	RA		
6	NF	PSNF3	NO	RA		
7	NF	PSNF3	NO	RA		
8	NF	PSNF3	YES	RA	US	78/22
9	NP1	PSNP3	YES	IA	US	69/31
10	NP1	PSNP3	YES	IA	US	82/18
11	NP1	PSNP3	YES	RA	US	62/38
12	NP1	PSNP3	YES	US	IA	54/46
13	NP1	PSNP3	NO	SA		
14	NP1	PSNP3	YES	SA	US	72/28
15	NP2	PSNP4	NO	RA		
16	NP2	PSNP5	NO	RA		
17	NP2	PSNP5	YES	RA	SA	88/12
18	NP2	PSNP5	YES	RA	SA	86/14
19	NP2	PSNP5	YES	RA	SA	88/12
20	NP2	PSNP5	NO	IA		
21	NP2	PSNP5	NO	IA		
22	NP2	PSNP5	YES	IA	US	75/25
23	NP2	PSNP5	YES	US	IA	59/41
24	NP2	PSNP5	YES	IA	US	67/33
25	NP2	PSNP5	NO	US		
26	NP3	PSNP6	YES	US	IA	82/18
27	TH	PSNP1	NO	RA		
28	TH	PSNP1	NO	US		
29	PEP1	PSPEP2	NO	IA		
30	PEP1	PSPEP2	YES	IA	US	90/10
31	PEP1	PSPEP2	YES	IA	US	78/22
32	PEP1	PSPEP2	YES	IA	US	68/32
33	PEP1	PSPEP2		NR		
34	PEP1	PSPEP2		NR		
35	PEP1	PSPEP3	NO	RA		
36	PEP1	PSPEP3	NO	RA		
37	PEP1	PSPEP5		NR		
38	PEP2	PSPEP1	NO	RA		
39	PEP2	PSPEP1	YES	RA	US	67/33
40	PEP2	PSPEP1	YES	RA	SA	58/42
41	PEP2	PSPEP1	NO	RA		
42	PEP2	PSPEP1	YES	RA	US	73/27
43	PEP2	PSPEP1	YES	IA	US	72/28
44	PEP2	PSPEP1	NO	SA		
45	PEP2	PSPEP1	YES	SA	RA	69/31
46	PEP2	PSPEP1	YES	US	RA	75/25
47	PEP2	PSPEP1	NO	US		
48	PEP2	PSPEP1	NO	SA		
49	PEP2	PSPEP1	YES	US	RA	67/33
50	PEP2	PSPEP1	NO	US		
51	PEP2	PSPEP1	YES	SA	RA	51/49
52	PEP2	PSPEP1	NO	US		
53	PEP2	PSPEP1	NO	US		

Supplemental Table 1. Summary of transcriptomics classification and mechanoelectrical properties of the scRNAseq neurons, related to Figure 3

RNA sequenced DRG neurons are labeled according to their genetically identified neuronal type and their MS currents characterized by patch clamp experiments. Mixed currents are MS currents for which inactivation kinetics could be fitted with bi-exponential function, revealing the presence of two distinct MS components, with the smaller (current type 2) contributing to at least 10% of the peak current amplitude.